EXPERIMENTAL IDENTIFICATION OF FORCE COEFFICIENTS OF HYBRID AIR FOIL BEARINGS

by

YU PING WANG

Presented to the Faculty of the Graduate School of

The University of Texas at Arlington in Partial Fulfillment

of the requirements

for the degree of

MASTER OF SCIENCE IN AEROSPACE ENGINEERING

THE UNIVERSITY OF TEXAS AT ARLINGTON

August 2012

ACKNOWLEDGEMENTS

I sincerely thank my committee chair, Dr. Daejong Kim, for his guidance and support. Dr. Kim's passion and dedication have been extremely inspirational and he keeps encouraging me to be more than just a student working in the Microtrubomachinery and Energy Systems Laboratory. I also want to thank my colleagues, especially JeongPill Ki, Shrikant Yadav, and Suman Shrestha for their friendship and participation in my research.

I want to express my gratitude to Kermit Beird from the UT Arlington machine shop specifically for his patience, assistance, and instructions as well as Dr. Robert Woods and Dr. Alan Bowling for their consent to be committee members.

Last but not least, I want to give my absolute appreciations for friends and families who have given me unconditional love and support throughout my academic years and thank God for his graciousness without which I would not be able to experience so much.

July 19, 2012

ABSTRACT

EXPERIMENTAL IDENTIFICATION OF FORCE COEFFICIENTS

OF HYBRID AIR FOIL

BEARINGS

Yu Ping Wang, MS

The University of Texas at Arlington, 2012

Supervising Professor: Daejong Kim

Successful applications for air foil bearings in small to midsize turbomahcinery have been acknowledged. Air foil bearings do not require oil lubricant thus they are capable of operating under much higher temperature than oil-lubricated bearings and they entail less maintenance costs if well-designed. However, when rotor size increases beyond 100 mm in diameter, reliability becomes an issue due to comparable increase in rotor weight with respect to increase in load capacity of the bearing. Furthermore, dry rubbing during starts and stops also causes concerns due to typical slow acceleration and deceleration characteristics of large turbomachinery.

The concept of hybrid air foil bearing was developed by Kim and Park to alleviate those concerns by introducing hydrostatic pressure inside the air film. Previous research on the hybrid air foil bearings indicates that hybrid air foil bearing can offer improvement in rotor stability and heat dissipation. In addition, significant reduction in dry friction at start/stop was also recorded from experimental investigations.

Rotordynamics behavior depends on bearing stiffness and damping coefficients. They can be determined analytically form linear perturbation method using Reynolds equation. However,

experimental identification for bearing force coefficients is critical in order to accurately classify and predict bearing performance under both normal and severe operating conditions.

This thesis presents stiffness and damping coefficients of 4” diameter hybrid air foil bearing. A test rig formerly used for characterization of start-stop transient response was used for the experiment. The original 4” diameter hybrid air foil bearing was refurbished to improve its performance and assembly procedure. A frequency-domain technique is used to identify dynamic characteristics of the hybrid air foil bearing from measured impulse response using least square method. The measured bearing coefficients are in reasonable agreement with prediction from linear perturbation method.

TABLE OF CONTENTS

ACKNOWLEDGEMENT……..iii

ABSTRACT……..……iv

LIST OF ILLUSTRATION…….....ix

LIST OF TABLES……xi

NOMENCLATURE…….xii

Chapter Page

1. INTRODUCTION……1

1.1 Foil air bearing 1

1.1.1 Principle of Operation 1

1.1.2 Classical Lubrication Theory 2

1.2 Hybrid air foil bearing (HAFB)..... 5

2. LITERATURE REVIEW AND OBJECTIVE 7

2.1 Temperature profile within foil bearing 7

2.2 Thermal management techniques 8

2.3 Radial clearance and bearing performance..... 9

2.4 Parametric study---top foil geometry and bump stiffness distributions..... 9

2.5 Parametric study---hybrid air foil bearing dynamic performance..... 10

2.6 Three-pad hybrid air foil bearing design---imbalance response, effect on load angle, and static performance 11

2.7 Three-pad hybrid air foil bearing start/stop characteristics and thermal behavior..... 12

2.8 Research Objective 14

3. DESIGN, MANUFACTURE, AND ASSEMBLY OF HYBRID AIR FOIL BEARING..... 15

3.1 HAFB Design 15

3.2 Description of HAFB Manufacturing Process 19

3.2.1 Bearing holder 19

3.2.2 Bearing sleeve 19

3.2.3 Bottom foil 20

3.2.4 Corrugated bump foil 23

3.2.5 Top foils 25

3.2.6 Orifice tubes 25

3.3 HAFB Assembly 27

4. IMPULSE EXCITATION TEST RIG 31

4.1 Test rig set up 33

4.2 Measuring devices and data acquisition set up 36

5. METHODOLOGY 39

5.1 Least square method for identification of bearing characteristics 39

5.2 Least square method for 2DOF system 40

5.3 Application of least square method on 2DOF simulated vibration signal 43

5.4 General experimental approach 47

5.5 Modification to experimental procedure 50

5.5.1 PCB Impact Hammer 50

5.5.2 Signal Process 50

5.5.3 Bearing Assembly Axial Constraints 52

6. RESULTS AND DISCUSION 53

6.1 Purposes of the experiments 53

6.2 Dynamic bearing force coefficients 53

7. CONCLUSION AND FUTURE WORK 66

APPENDIX

A. MULTIVARIABLE REGRESSION…… 68

B. DATA ACQUISITION WITH LABVIEW……... 70

REFERENCES…….. 73

BIOGRAPHICAL INFORMATION…… 74

LIST OF ILLUSTRATIONS

Figure Page

1.1 General Foil Air Bearing Components. 2

1.2 Cartesian Coordinate System for Fluid Film. 3

3.1 Complete HAFB Assembly. 16

3.2 Complete HAFB Assembly. 17

3.3 Bearing holder and Complete Bearing assembly. 20

3.4 Top and Bottom Foil Forming Jig (a) complete forming jig and
(b) bottom portion of forming jig showing top foil fixed end contour. 21

3.5 Manufactured Bottom Foil with Bump Foil. 22

3.6 Hydraulic Press for Cold Forming Process. 22

3.7 Electric Furnace for Foil Heat Treatment. 23

3.8 Bump Foil Forming Jig. 24

3.9 Spot Weld Location of Bump Foils. 24

3.10 Solid Model of Orifice Tube. 26

3.11 Incision Marks on Top Foil. 26

3.12 Orifice Tube Interference with Bearing Sleeve. 27

3.13 Bearing Sleeve Constraint Mechanism showing (a) HAFB assembly
front end and (b) HAFB assembly rear end. 28

3.14 Thermal Couple Wire Attachment. 29

3.15 Thermal Couple Wire Relay. 30

3.16 Top and Bottom Foil Assembly. 30

4.1 HAFB Test Rig. 33

4.2 HAFB Reference Frame. 34

4.3 HAFB Orientation With Respect to Rotor Spin. 35

4.4 Applied Load and Loaded Pad. 35

4.5 Oil Mist Lubricant Access Alignment. 36

4.6 Proximity Probe Calibration Curve for (a) vertical proximity sensor and (b) horizontal proximity sensor. 37

4.7 PCB Impact Hammer. 38

5.1 2DOF mass spring damper system. 40

5.2 Vibration response of 2DOF system due to external force applied in x-direction. 44

5.3 Vibration response of 2DOF system due to external force applied in y-direction. 44

5.4 Amplitude plot of 2DOF system. 45

5.5 HAFB Baseline Signals at 15000 RPM. 49

5.6 HAFB Impulse Response at 15000 RPM. 50

5.7 Data Process Scheme. 52

6.1 Vibration Response Due to X Impulse Excitation at 18k Rpm and 4.83 Bar Supplied Pressure. 54

6.2 Vibration Response Due to Y Impulse Excitation at 18k Rpm and 4.83 Bar Supplied Pressure. 55

6.3 Identification Results for HAFB Direct and Crosscoupled Stiffness Coefficient showing (a) Kxx, (b) Kxy, (c) Kyx, and (d) Kyy. 57

6.4 Identification Results for HAFB Direct and Crosscoupled Damping Coefficient showing (a) Dxx, (b) Dxy, (c) Dyx, and (d) Dyy. 58

6.5 Experimental Vibration Response of HAFB at 18k Rpm and 70 Psi Supplied Pressure. 60

6.6 Simulated Vibration Response of HAFB Using Experiment Force Coefficients. 60

6.7 Fourier Transform Magnitude Plot of the Experimental Vibration Response. 61

6.8 Fourier Transform Magnitude Plot of the Simulated Vibration Response. 61

6.9 Fourier Transform Phase Plot of the Experimental Vibration Response. 62

6.10 Fourier Transform Phase Plot of the Simulated Vibration Response. 62

6.11 HAFB Static Deformation Curve. 64

LIST OF TABLES

Table Page

3.1 Design Specification of three-Pad HAFB 18

5.1 Least square method stiffness, mass and damping of 2DOF system 46

5.2 Frequency range 50 Hz to 80 Hz 46

5.3 Frequency range 20 Hz to 60 Hz 46

5.4 Frequency range 120 Hz to 160 Hz 47

6.1 HAFB Stiffness, Mass, and Damping properties 56

6.2 HAFB Static Stiffness 64

NOMENCLATURE

C	Bearing radial clearance in [m]
d	Hybrid air foil bearing damping coefficient with firs subscript representing direction in Cartesian coordinate and second subscript representing bearing response
$F_{friction}$	Force due to friction [N]
f	Excitation force [N]
h	Local fluid film thickness in [m]
k	Hybrid air foil bearing stiffness coefficient with firs subscript representing direction in Cartesian coordinate and second subscript representing bearing response
p	Absolute pressure within fluid film
P	Non-dimensionalized pressure
t	Time measured in second
W_{load}	Bearing load capacity [N]
u, v, w	Air flow speed within the film
x, y, z	Fluid flow Cartesian coordinate defined with x along bearing circumferential direction, y across film thickness, and z along bearing axial direction

X, Y, Z	Non-dimensionalized fluid flow Cartesian coordinate for introduction of Reynold's equation and are later defined as reference frame for the bearing assembly with X representing the vertical axis, Y representing the horizontal axis, and Z representing axis along the length of the bearing assembly
τ	Non-dimensionalized time
μ	Air dynamic viscosity [$N \cdot s / m^2$]
ω	Rotor speed in [rad / s]

CHAPTER 1

INTRODUCTION

Foil bearing technology using air or gas as a lubricant has been around for about half a century since the mid 60's and it has made significant progress in terms of reliability. The foil bearings for Air Cycle Machine (ACM) onboard Boeing 747 aircraft have exhibited remarkable operating endurance capability above 100,000 hours [1]. Foil bearings have several advantages in comparison to oil-lubricated bearings. By replacing oil lubrication system with foil bearings, operating cost is reduced with less frequent scheduled maintenance. Due to their geometric characteristics with small clearances between the bearing and shaft and shock-tolerances, foil bearings provide minimal damage to the system while restraining the shaft assembly from vibrating excessively during failure. Rolling element bearings require lubricating oil which typically suffers thermal degradation at temperatures beyond approximately 200 degree Celsius and becomes ineffective. On the other hand, foil bearings uses air/gas as a lubricant that does not thermally degrade. As a result, foil bearings' thermal constraints only depend on temperature limits and thermal expansion of the chosen material of the bearing and the rotor assembly.

1.1 Foil air bearing

1.1.1 Principle of Operation

Figure 1.1 shows general configuration of the foil bearing with continuous top and bump foils along with the direction of shaft rotation. The fundamental mechanism of foil bearings comprises of one or multiple pads of compliant and smooth surfaces called top foil which forms a wedge-shaped radial clearance with the rotor surface. When the shaft rotates, relative motion of the two surfaces generates hydrodynamic pressure that carries the load. The generated pressure keeps the top foil from the shaft surface, and hence the shaft becomes fully airborne and the friction loss becomes negligible. Corrugated bump foils are commonly used as a stiffness element to

accommodate shaft run-out and misalignment as well as to provide cooling air flow passage which further enhances foil air bearing performance. Sliding friction between the top foil and bump foil and between the bump foil and sleeve creates coulomb damping that is essential for machine stability.

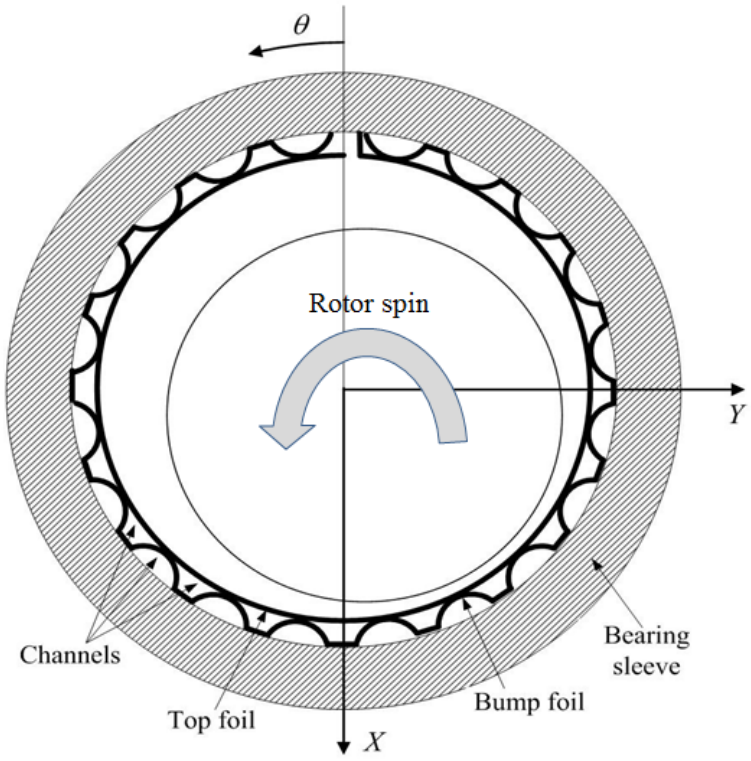

Figure 1.1 General Foil Air Bearing Components.

1.1.2 Classical Lubrication Theory

All of the analytical studies performed on foil air bearings are based on the classical lubrication theory derived by Osborne Reynolds in 1886. Pressure profile within the fluid film can be solved using Reynolds equation which can then be used to determine bearing performance and characteristics. A brief derivation for the Reynolds equation is presented here for introductory purpose to show theory and assumptions behind how foil bearings operate, though application of Reynolds equation is not part of the focus within the scope of this research.

Several assumptions are taken into consideration for general fluid film bearings. The fluid flow is assumed to be laminar due to low Reynolds number and therefore fluid body and inertia forces are negligible. Since the clearance between the rotor and the bearing are so miniscule the pressure across the thin fluid film is assumed constant and curvature effects due to geometric shape of the bearing can also be neglected. Finally, the fluid inside the bearing is assumed to be Newtonian so fluid viscosity should be constant.

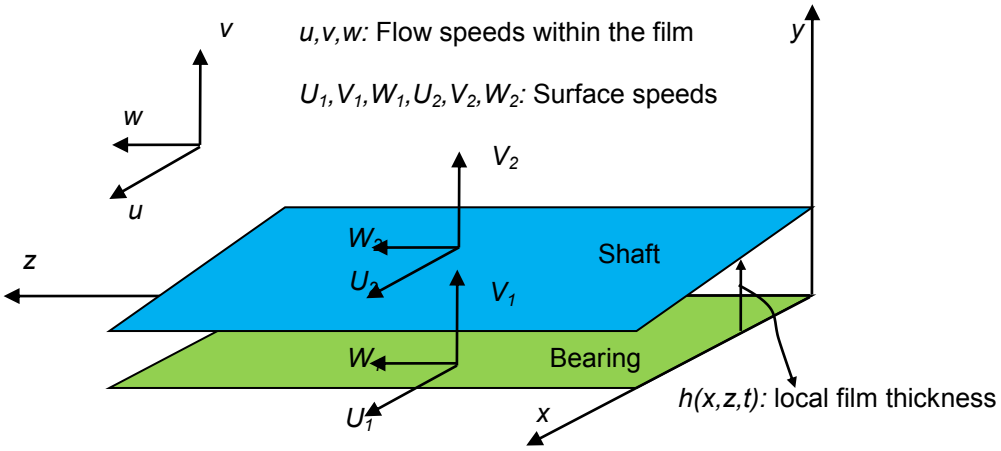

Figure 1.2 Cartesian Coordinate System for Fluid Film.

Consider two sliding surfaces defined in Cartesian coordinate system in Figure 1.2. Standard Navier Stokes equation in three dimensions and some definitions for non-dimensional parameters that can be utilized to simplify the derivation are expressed below.

$$\begin{aligned}
\rho\left(\frac{\partial u}{\partial t}+u\frac{\partial u}{\partial x}+v\frac{\partial u}{\partial y}+w\frac{\partial u}{\partial z}\right)&=-\frac{\partial p}{\partial x}+\mu\left(\frac{\partial^2 u}{\partial x^2}+\frac{\partial^2 u}{\partial y^2}+\frac{\partial^2 u}{\partial z^2}\right)\\
\rho\left(\frac{\partial v}{\partial t}+u\frac{\partial v}{\partial x}+v\frac{\partial v}{\partial y}+w\frac{\partial v}{\partial z}\right)&=-\frac{\partial p}{\partial y}+\mu\left(\frac{\partial^2 v}{\partial x^2}+\frac{\partial^2 v}{\partial y^2}+\frac{\partial^2 v}{\partial z^2}\right)\\
\rho\left(\frac{\partial w}{\partial t}+u\frac{\partial w}{\partial x}+v\frac{\partial w}{\partial y}+w\frac{\partial w}{\partial z}\right)&=-\frac{\partial p}{\partial z}+\mu\left(\frac{\partial^2 w}{\partial x^2}+\frac{\partial^2 w}{\partial y^2}+\frac{\partial^2 w}{\partial z^2}\right)
\end{aligned} \tag{1}$$

$$P = \frac{pC^2}{\mu \bar{U} R}; \qquad X = \frac{x}{R}; \qquad Y = \frac{y}{C}; \qquad Z = \frac{z}{R}$$

$$U = \frac{u}{\bar{U}}; \qquad V = \frac{R}{C}\frac{v}{\bar{U}}; \qquad W = \frac{w}{\bar{U}}; \qquad \tau = \omega t; \qquad \bar{\mu} = \frac{\mu}{\mu_0} \tag{2}$$

$$\left(\frac{C}{R}\right)^2 << 0; \qquad \frac{\rho \bar{U} C}{\mu}\frac{C}{R} << 1; \qquad \frac{\rho C^2 \omega}{\mu} << 1 \tag{3}$$

After substitution of equation (2) into equation(1), several terms become significantly small as indicated in equation (3) and they can be neglected. Because pressure across the film is assumed to be constant ($\frac{\partial p}{\partial y} \cong 0$), Navier Stokes equation is then simplified and rearranged.

$$\mu \frac{\partial^2 u}{\partial y^2} = \frac{\partial p}{\partial x}; \qquad \frac{\partial^2 v}{\partial y^2} = 0; \qquad \mu \frac{\partial^2 w}{\partial y^2} = \frac{\partial p}{\partial z} \tag{4}$$

$$\frac{\partial \rho}{\partial t} + \frac{\partial \rho u}{\partial x} + \frac{\partial \rho v}{\partial y} + \frac{\partial \rho w}{\partial z} = 0 \tag{5}$$

The velocity profile can be determined from integration of the momentum equation (4) along with boundary conditions defined at the boundary surfaces. Velocity fields are then substituted into continuity equation (5) and integrated across film thickness to derive Reynolds equation. For incompressible flow where density is uniform, Reynolds equation for general fluid film lubrication is expressed in equation(6).

$$\frac{\partial}{\partial x}\left(\frac{h^3}{12\mu}\frac{\partial p}{\partial x}\right) + \frac{\partial}{\partial z}\left(\frac{h^3}{12\mu}\frac{\partial p}{\partial z}\right) = \frac{U_1 + U_2}{2}\frac{\partial h}{\partial x} + \frac{W_1 + W_2}{2}\frac{\partial h}{\partial z} + \frac{\partial h}{\partial t} \tag{6}$$

Where U_1 and U_2 are the velocity components of the sliding surfaces along the direction of the flow; W_1 and W_2 are velocity components of the sliding surfaces perpendicular to the direction of the flow. The LHS of equation (6) represents Poiseuille term which describes net flow rate due to pressure gradients. The first term on the RHS represents Couette term which

describes net flow rate due to shear. The second and third terms on the RHS each represents effects due to normal squeeze and local expansion respectively. Iterative methods can be implemented to solve for pressure, p, as well as film thickness, h, where they are then used to evaluate bearing characteristics and performance. For example load carrying capacity can be obtained by integrating pressure over the bearing surface and friction force can be obtained by integrating shear stress over rotor surface (see equation (7) and (8))

$$W_{load} = \int_A p dA = \int_{z=0}^{L} \int_{x=0}^{B} p dx dz \tag{7}$$

$$F_{friction} = \int_A \tau_{yx} dA = \int_{z=0}^{L} \int_{x=0}^{B} \tau_{yx} dx dz \tag{8}$$

1.2 Hybrid air foil bearing (HAFB)

The early implementation of foil bearing was generally limited to relatively small size turbomachinery with shaft power below 500 kW such as Air Cycle Machines, small turbocompressors/blowers, and micro gas turbines below 200kWe because they typically operate under low specific loads (load/bearing area) [2, 3]. However, as engine size and operating temperature increase such as in the small aircraft gas turbine engines, rubbing and wear due to heavy rotor weight can occur within the system. In addition, thermal management of the foil bearings in the small gas turbine engines is challenging. It is shown that the rotor weight increases significantly faster than bearing load capacity as the rotor characteristic dimension increases [4]. Therefore, research has indicated that conventional hydrodynamic foil bearings become unreliable as the bearing journal diameter exceeds 100 mm or roughly 4 inches [5].

In order to prevent dry rubbing at start/stops and enhance heat dissipation, hydrostatic bearings and magnetic bearings have been suggested as replacements to conventional foil air bearings. However, the applications of magnetic bearings are limited due to their significant

design challenges in terms of obtaining full active control [4]. Hybrid air foil bearing (HAFB) designed by Dr. Kim [6] is an example of hydrostatic gas bearing that combines the inherent hydrodynamic pressure of a conventional foil air bearing with hydrostatic lift provided by pressurized air through orifices attached on the top foil. According to experimental studies [6] HAFB has better load capacity and heat dissipating capability. The hybrid operation reduces cross coupling stiffness and improves rotor stability [4]. In addition, supplied air carries excessive heat out of the system and improves heat dissipation.

CHAPTER 2

LITERATURE REVIEW AND OBJECTIVE

This chapter presents summary of past relevant research on foil bearings and hybrid foil bearings with information pertaining to bearings' characteristics as well as influential factors such as physical parameters, material properties, and thermal behavior that dictate bearing performance. The literature review presented in this chapter also facilitates the following purposes; validate current hybrid air foil bearing design, provide guidance for experiments conducted for this research, and offer justifying comparison between previously evaluated bearing characteristics and results obtained from this experimental study. Furthermore, Research objectives are introduced at the end of this chapter.

2.1 Temperature profile within foil bearing

This section summarizes the work by Radil and Zeszotek [2].

Experimental studies and simulations of foil air bearings were conducted to improve and ensure their superior reliability in comparison to rolling element counterparts. Bearing stiffness and damping characteristics are closely related to bearing performance and bearing temperature has significant effects on force coefficients. Consequently, it is essential to be able to obtain and understand the temperature profile within the foil bearing under operation. Radil and Zeszotek [2] performed an experimental investigation of a compliant foil air bearing to acquire temperature profile within the bearing during operation. Three sets of three thermocouples were positioned along the circumference of the bearing surface with each set located on the edges and in the middle of the bearing surface. Local temperature data was collected to monitor both axial and circumferential thermal gradient as a function of load and rotor speed at room temperature. The authors point out the bearing internal temperature depends on three factors- compression work done on fluid, operation environment, and heat energy generated due to viscous shearing in the

thin air film. Heating of the air film in this condition becomes dominant because of high rotor speed and tight clearance ($\sim 10\mu m$). Because air has comparably low heat capacity, most of the heat energy generated within the system is then absorbed by the surrounding surfaces which then lead to possible bearing failure. The experimental data indicated that both radial load and rotor speed can affect heat generation with rotor speed being the dominant factor. Counter intuitively, the results also exhibited maximum temperature located in the middle of the bearing where maximum air film thickness was assumed to be thicker while circumferential thermal gradient became negligible. It was speculated that due to insufficient pressure gradient for complete exchange for the air entering and exiting the system, circumferential flow in the middle was trapped and continuously heated. Later analytical simulation model further justified the hypothesis.

2.2 Thermal management techniques

This section summarizes work by Radil et al [3].

Radil et al [3] further conducted experiments to assess the effectiveness of three thermal management techniques for oil free turbomachinery systems. Foil bearing performance characteristics such as load capacity, stiffness, and damping depend on the material properties of bearing support structure. Regardless of superior durability of nickel-based super alloy at high temperature, elastic foundation may deteriorate when temperature exceeds $650℃$ due to reduction in air film thickness at higher load. In addition, thermal gradient within the bearing raises another issue when designing foil air bearing. In retrospect, circumferential air flow midway through the bearing assembly is constantly heated by viscous shearing. Through heat conduction between air film and bearing structure, local thermal distortion may also results in bearing failure. Direct and indirect shaft cooling experiments were conducted using hollow shaft with cooling air transmitted through inner guide tube. The concept behind these two techniques dissipates heat energy through conduction from air film into the journal then transmits the heat from journal into cooling air through convection out of the system. These techniques maintain radial clearance

while limit thermal expansion of the shaft. The third approach which was determined to be the most effective utilized a more common technique by introducing cooling air axially through bump foils.

2.3 Radial clearance and bearing performance

This section summarizes the work by Radil et al [7].

Radial clearance of foil air bearing is one important design parameter that represents space allowed for shaft radial movement. In gas lubricated bearings, radial clearances are very small that there is hardly any perceivable gap when the shaft is at rest. They consist of residual gap within the bearing elastic structure or existing small spaces where top foils do not completely conform to the shaft. Radial clearance is typically measured by load deflection test with dial indicators. It is absolutely crucial to study and understand the effects of changes in radial clearance since it plays a very significant role in terms of bearing performance and elastic properties. Radil et al [7] conducted load capacity tests to determine how the variations in radial clearance affect bearing performance. It was reported that insufficient radial clearance causes problems with difficult shaft-bearing assembly, requirement for excessive start-up torque, and reduction in load capacity while, on the other hand, too much radial clearance also results in reduction in load capacity as well as system instability. Consequently, there appears to be an optimal radial clearance differentiating two distinct operating characteristics. The study concluded dramatic reduction in load capacity and system suffers thermal runaway and bearing seizure when radial clearance is less than optimum where 20% reduction in bearing capacity without thermal issues was recorded with radial clearance larger than optimum.

2.4 Parametric study---top foil geometry and bump stiffness distributions

This section summarizes work by Kim [8].

Earlier analytical studies on foil air bearings assumed bearings with identical bump stiffness distribution. In order to gain further insights of foil air bearing operating fundamentals, Kim [8] conducted parametric studies to investigate the impacts on bearing static and dynamic

performance with variations in both bearing geometry and bump stiffness distribution. Two subcategories were established for this study; 1) configuration with one continuous circular top foil and one continuous circular bump foil, and 2) configuration with three top foil pads with each pad being hydrodynamically preloaded. The two bearing subcategories were further divided by 1) uniform bump stiffness and 2) parabolic stiffness profile along both axial and circumferential direction. The report indicated insignificant effects of stiffness distribution on the bearing load capacity and stability characteristics, while the top foil geometry has more significant effect on load capacity and stability. Due to high air film viscosity combined with low air heat capacity, thermal issues become the dictating factor in terms of bearing load capacity. Bearing dynamic performance was examined by perturbation method to determine frequency-dependent force coefficients. There were no substantial changes in bearing stiffness among different bump stiffness distribution. However, eminent reduction in synchronous force coefficients, particularly cross coupled stiffness, was recorded among the two bearing geometries at high speed. In addition, time domain orbit simulations were carried out to examine the stability performance of circular continuous configuration and three pad configuration. Higher onset speed of instability was recorded for three pad preloaded configuration signifying superior stability in comparison to circular continuous bearing.

2.5 Parametric study---hybrid air foil bearing dynamic performance

This section summarizes work by Kim and Park [6] and Kim and Kumar [9].

As external load increases, reliability issue caused by dry rubbing at start/stops and poor heat dissipating capability becomes inevitably significant. Hybrid Air Foil Bearing (HAFB) concept was first introduced by Kim and Park [6] as a remedy to address this particular concern. In the conventional design for foil bearings, the cooling passages are located behind top foils and could not provide efficient cooling to the rotor which undergoes thermal distortion due to convection from heat generated within the fluid film. The HAFB concept proposes the idea to deliver externally pressurized air into the bearing clearance to provide cooling for both the bearing and

rotor surfaces. In addition to enhanced cooling, HAFB also reduces incidence of dry rubbing at start/stops. Kim and Kumar [9] developed linear perturbation method for HAFB to evaluate bearing force coefficients. The investigation also reported how force coefficients varies with changes in HAFB design parameters---supplied pressure, feed parameter (function of air supply orifice diameter), excitation frequency, and bearing number (function of rotational speed). The results showed that the direct and cross coupled stiffness are reduced while direct and cross coupled damping rises when either supplied pressure or feed parameter is increased. This indicates that the externally pressurized air fed into the fluid film can be regulated to provide rotor stability. Furthermore, rapid decrease in direct and cross coupled damping as well as cross coupled stiffness were predicted at super-synchronous excitation frequency while direct stiffness showed increasing trend with the excitation frequency. Due to the gas hardening effect of gas bearing, super-synchronous excitation should be avoided considering loses in damping with high stiffness values. Finally, the effects of increase in bearing number on force coefficients were similar to those predicted for increasing excitation frequency.

2.6 Three-pad hybrid air foil bearing design---imbalance response, effect on load angle, and static performance

This section summarizes the work by Kim and Lee [4].

One potential application of hybrid air foil bearings is their utility in airborne military engines considering the advantage being able to operate at higher speed and temperature. Rotor-bearing stability becomes a major concern due to large rotor mass thus, three pad preloaded HAFB configuration becomes an obvious choice. Extending earlier effort on the parametric study mentioned previously, Kim and Lee [4] developed a time-domain orbit simulation for stability analysis varying angles of the load vector with respect to rotor axis. The frequency-domain linear perturbation method was also used for identification of the bearing force coefficients as well as natural frequency of the rotor-bearing system. It was predicted that hybrid air foil bearing has higher onset speed for instability when compared to hydrodynamic foil bearings. The effect on

changes in load angle raises concerns for instability when the bearing is lightly loaded or when the load direction is not perpendicular to the rotor axis and the magnitude for subsynchronous vibration gets worse as load angle decreases. Hybrid air foil bearing does provide stability up to higher speeds for all load angles compared to hydrodynamic air foil bearing. However, while the magnitude of the onset subsynchronous vibrations were insignificant compared to the synchronous vibration the simulation indicated that they grow rapidly and become unbounded as speed increases. Frequency-domain perturbation analysis suggests that modification on either the feed parameter or supplied pressure can help improve rotor stability when load angle and operating speeds are taken into consideration during bearing design stage. To confirm results predicted using perturbation method, an experimental study was also performed to estimate the hybrid air foil bearing stiffness when the rotor is at stationary. It was shown that the bearing stiffness increases with applied external load.

2.7 Three-pad hybrid air foil bearing start/stop characteristics and thermal behavior

This section summarizes the work by Kim and Zimbru [10].

In retrospect, concern for stability issue was mentioned earlier for potential application of hybrid air foil bearing in aspect of aero-propulsion where bearing undergoes dynamic external loading due to constant changes during aircraft maneuvers. In aforementioned discussion, the thermal management as well as dry rubbing issues at start/stop were also brought up as bearing size increases. It was concluded that the combination of hydrodynamic effects with hydrostatic lifts (i.e. HAFB), does provide some favorable features that address these concerns. By using linear perturbation method, the results indicates reduction in cross coupled stiffness and escalation in direct damping when either feed parameter (orifice tube diameter) or supplied air pressure increases. The time-domain orbit simulation also shows higher onset speed for rotor instability with hybrid air foil bearing. Furthermore, the direct injection of cooling air into the bearing clearance through orifice tubes dramatically enhances cooling capability of the bearing. A test apparatus was constructed in The Microturbomachinery and Energy Systems Laboratory led

by Dr. Daejong Kim at the University of Texas, Arlington to study the hybrid air foil bearing's thermal behavior as well as its start/stop characteristics. Similar test apparatus and bearing configurations detailed in the following section are also used for the purpose of this thesis work. Kim and Zimbru [10] performed experiments to measure friction torque primarily due to dry rubbing at start-up to 2000 rpm with controlled acceleration 13 rev/s^2 under various radial loads from 225N to 400N. Knowing applied load from the motor and bearing radius, friction coefficient can be calculated by dividing load cell measurements (friction torque) by applied load and bearing radius. Comparing the results with high speed small commercial hydrodynamic foil bearing, HAFB significantly outperforms in terms of friction coefficient (0.0009 at 400N load for HAFB compared to 0.605 for hydrodynamic foil bearing). Transient thermal behavior was investigated at 4000, 6000, 8000 and 10k rpm with constant 445N external load while monitoring and maintaining upstream air regulator pressure and total air flow rate through orifice tubes. Unlike hydrodynamic foil bearings (referring to 1.3.1), temperature readings at the bearing center are significantly lower than temperature readings around the edge of the bearing since cooling air is directly injected at the bearing center. Roughly 15 C° increase in temperature at the bearing edge was recorded at steady state for both 6k and 8krpm which may suggest least friction. Rise in temperature was also measured at 8k and 10krpm while adjusting upstream regulator pressure from 5.52 to 2.07 bar. Experiments were terminated at roughly 2.07 bar at the regulator when temperature could not reach steady state within a specified period of time. This may serve as experimental guideline for required upstream regulator pressure. Finally, an endurance test was conducted under 356 N load and 4.48 bar at the regulator with rotor accelerating/decelerating at 6 rev/s^2. Rubbing wears were identical to the initial break-in marks after 200, 400 and 1000 start/stop cycles, suggesting no more significant rubbing after the initial break-in period.

2.8 Research Objective

Based on research outcomes presented in the previous section and past experimental experience [Kim and Zimbru [10], the three-pad hybrid air foil bearing was refurbished to improve assembly procedure and overall performance of the bearings. This thesis includes manufacturing process and configuration of the bearing as well as test apparatus set-up for the two degrees of freedom (DOF) rotordynamics system.

There exists numerous types of fluid film bearings or foil bearings, and each particular bearing is designed for a particular application under specific operating conditions. Hybrid air foil bearing combines hydrodynamic effects with hydrostatic lifts, and is designed for its potential application in small aero-propulsion engines or large turbomachinery applications. Experimental determination of bearing force coefficients (stiffness and damping coefficients) is crucial. Due to limited understanding of operating fundamentals of fluid film bearings as well as analytical computing tools, experimental identification of bearing characteristics helps to verify analytical results as well as to predict bearing performance under both standard and extreme operating conditions [11, 12]. The objective of this research is to develop a method to identify force coefficients of hybrid air foil bearing from measured impulse response.

The results are first confirmed with the identification method by implementing simulated rotor impulse response for a 2 DOF system. Test apparatus is then arranged to acquire vibration signal with proximity probes. Dynamic bearing characteristics are identified with measured impulse response due to impact excitations. This paper includes detailed introduction to the identification method, experimental procedure, measured input/response, signal processing method, and estimated stiffness and damping coefficients.

CHAPTER 3

DESIGN, MANUFACTURE, AND ASSEMBLY OF HYBRID AIR FOIL BEARING

The motivations behind the concept for hybrid air foil bearing are to address dry-rubbing issue during rotor start/stop and to provide sufficient heat dissipation while providing desired load capacity as well as rotor stability. The previous work summarized in Section 2.2 suggests that bearing performance characteristics such as load capacity, stiffness, and damping depend on material properties of the bearing support structure, which is subjected to thermal distortion under poor heat dissipation. Per literature reviewed in Section 2.1, the maximum temperature occurs at the center of the bearing. Based on the findings, it is justified to inject externally pressurized air at locations where maximum heat generation exists. Previous experimental work in Section 2.7 demonstrated successful endurance test up to 1000 start/stop cycle using the same hybrid air foil bearing configuration and test facility. Furthermore, results from parametric studies presented in section 2.4 and 2.5 indicate reduction in cross-coupled stiffness of HAFB and higher onset speed for instability.

3.1 HAFB Design

Figure 3.1 shows the isometric view of the complete hybrid air foil bearing assembly. The HAFB is designed based on three-pad configuration with each pad consisting of one top foil, one bottom foil, and a series of corrugated bump foils laid in between. From the literature review presented in Section 2.4, although bump stiffness distribution do not play significant role in terms of load capacity, bearing geometry contributes substantial effects on stability, i.e., the three-pad bearing configuration predicts higher onset speed for instability. Therefore, three-pad HAFB design was chose for the current thesis.

Figure 3.1 shows the cutaway exploded view of HAFB showing the location of the injected air indicated by white arrows on top and bottom foil. Note that foil should be attached to the back

side of the top foil at the air injection point. For ease of assembly, bottom foils are divided into two portions at the injection point as will be explained in detail in the assembly section. Physical dimension of the hybrid air foil bearing is presented in Table 3.1.

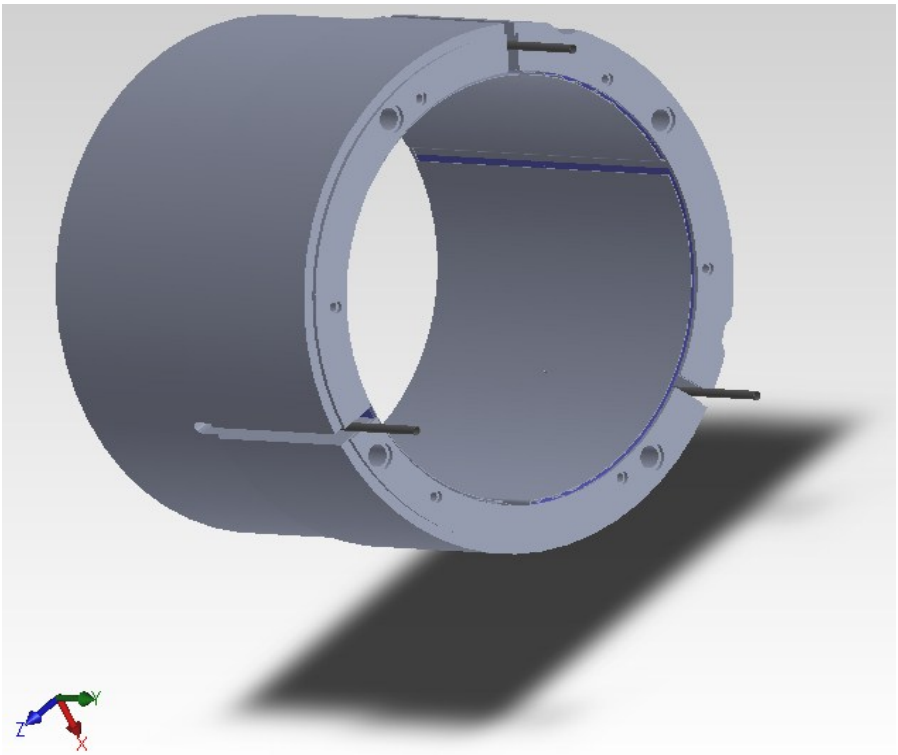

Figure 3.1 Complete HAFB Assembly.

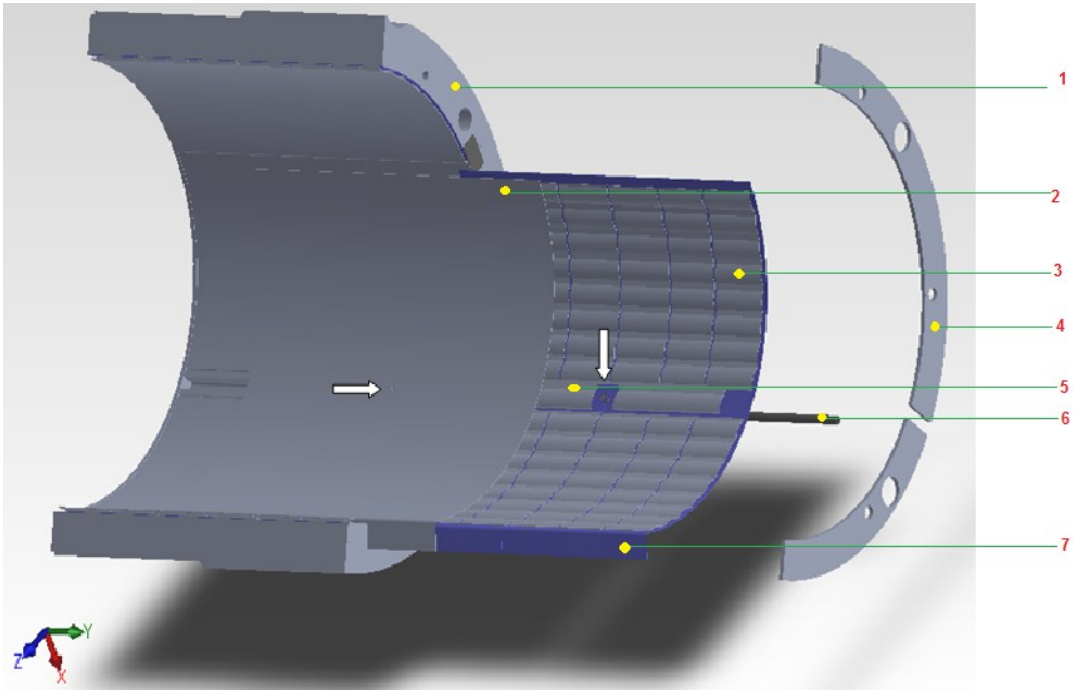

Figure 3.2 Complete HAFB Assembly.

Description of each component presented in Figure 3.2 is listed below.

1. Bearing sleeve--- Three slits located at equal distance apart along the circumference are cut with tight tolerance for the assembly of the top and bottom foil onto the bearing holder.
2. Top foil--- Fixed end is located at the assembly point allowing the free end to slide freely as the bearing gets loaded and unloaded. Angular span for each top foil from fixed end to free end is $118°$. Rotor spin direction is always from the free end to the fixed end.
3. Bump foil--- HAFB elastic structure that is free to stretch under load.
4. End plates--- They sit on top of the slits to prevent the top and bottom foils from sliding out of the bearing.

5. Bump shim--- One bump shim is located on each portion of the bottom foil along the vicinity where orifice tube is attached to the top foil to prevent the top foil from sagging when loaded.
6. Orifice tube--- They are laser welded onto the top foil.
7. Bottom foil--- They are part of the modification added to the previous design. HAFB can be easily assembled with pieces of bump foils spot welded onto single piece of bottom foil.

Table 3.1 Design Specification of three-Pad HAFB

Bearing Parameter	Nominal Value
Bearing diameter	104.04 mm (4.096 in.)
Bearing length	82.55 mm (3.25 in.)
Pad preload offset	30 μm (1.18 mils)
Set bore radial clearance	95 μm (3.74 mils)
Stiffness per unit area of bump foil	20 GN / m^3
Total number of orifices	3
Orifice diameter	1.7 mm
Bump heights	Varies within 5% of average
Bump foil thickness	6 mils (center) & 5 mils (bearing edge)
Bottom foil thickness	5 mils
Top foil thickness	8 mils

3.2 Description of HAFB Manufacturing Process

The complete hybrid air foil bearing assembly studied consists of following components---

- Bearing holder
- Bearing sleeve
- Bottom foil
- Corrugated bump foil
- Top foil
- Orifice

3.2.1 Bearing holder

Bearing holder is made of stainless steel 316. The outer diameter of the bearing sleeve is 4.999 in. and the inner diameter of the bearing holder is machined to 5.000 in. for interference fit between bearing sleeve and bearing holder. The primary purpose of bearing holder is to allow loading mechanisms to be attached to the bearing assembly. A partial 3/8” notch is machined on one edge of the bearing holder to match with the remaining portion of the 3/8’ notch machined on one edge of the bearing sleeve. A screw is set in the matching notch to restrict circumferential and axial sliding motion of the bearing sleeve in and out of the bearing holder. Figure 3.3 shows photo of bearing holder and complete bearing assembly with red arrows indicating the matching notch on bearing holder and bearing sleeve. For experiment purpose, additional screw sockets indicated by green arrows are tapped on the bearing holder positioned for preload torque rod as well as points of applied external load.

3.2.2 Bearing sleeve

Bearing sleeve is made of the same material as bearing holder. As previously mentioned in section 2.7, three slits are cut at equal distance apart along the circumferential direction on the bearing sleeve to house each set of the top and bottom foil. Six additional slits on each side of the thermal couples shown in Figure 3.3 were fabricated previously in the earlier design to

accommodate six bump foils lying beneath the top foil. Spot welding of pieces of bump foils onto bottom foil added in the new design is to simplify bearing assembly. Bearing sleeve inner diameter is expanded to accommodate the additional bottom foil thickness. Also shown in Figure 3.3 is the opening fabricated half way across the bearing sleeve next to the aforementioned notch. There are a total of three openings like this on the bearing sleeve to position orifice tubes within the housing thickness to eliminate interference.

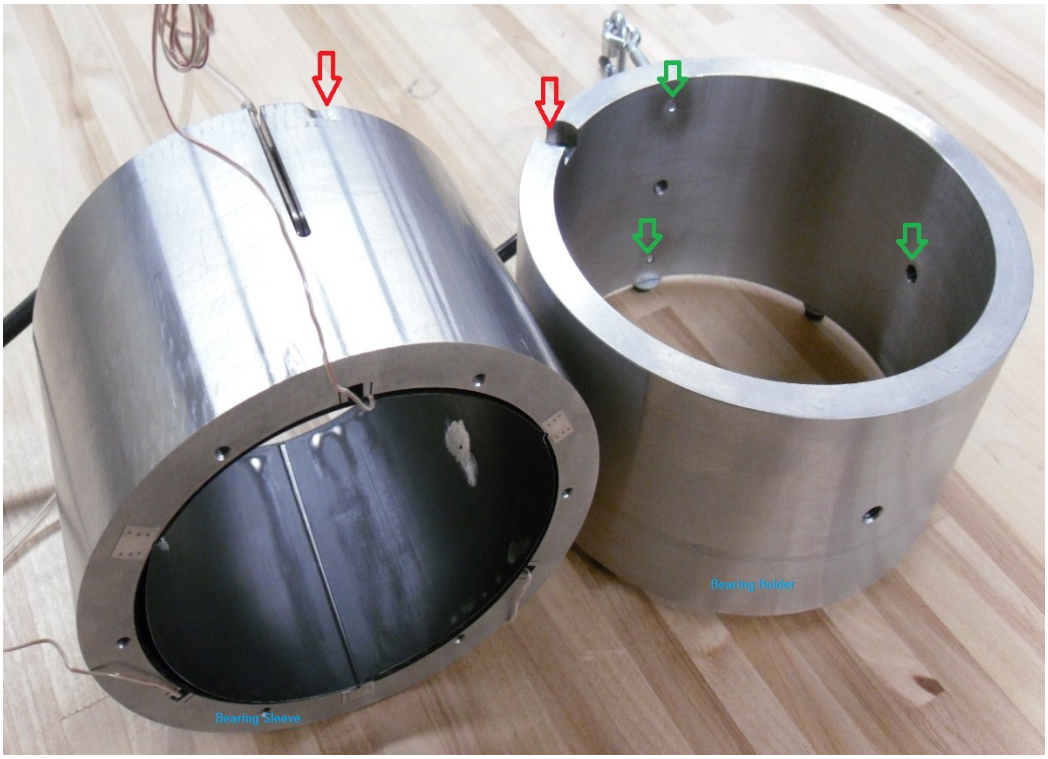

Figure 3.3 Bearing holder and Complete Bearing assembly.

3.2.3 Bottom foil

There are a total of six bottom foils constructed out of 5 mils thick Inconel 750 and they go through heat treat at $750°C$. Bottom foils and top foils are made with the same forming jig shown in Figure 3.4 and the purpose of the bottom foil is for spot welding of the bottom foil. Note that orifice tubes are attached onto the top foil and to avoid intervention between orifice tubes and bottom foil as well as ease of assembly, bottom foils are manufactured into top and bottom

portions separately. Underneath each top foil, there are two matching bottom foils with half circle slightly larger than the diameter of the orifice tube cut away along the inner edge. Figure 3.5 shows manufactured matching bottom foils with spot welded bump foils. All of the foils constructed are cold formed in the forming jig under a hydraulic press shown in Figure 3.6 and they are sent to heat treat in furnace shown in Figure 3.7.

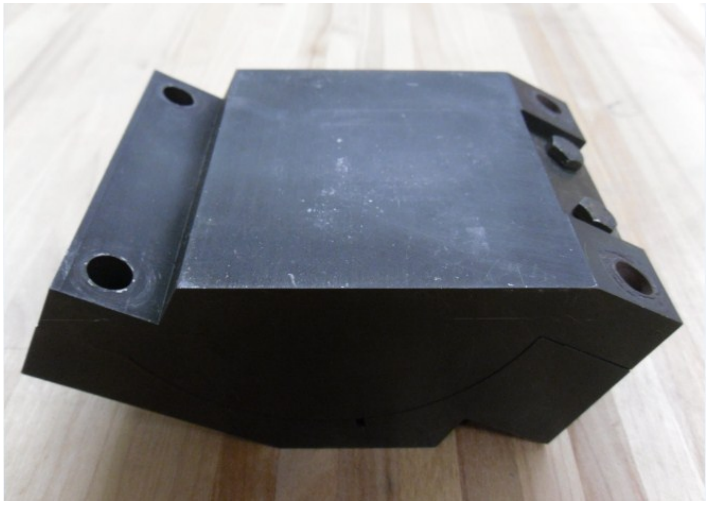

(a)

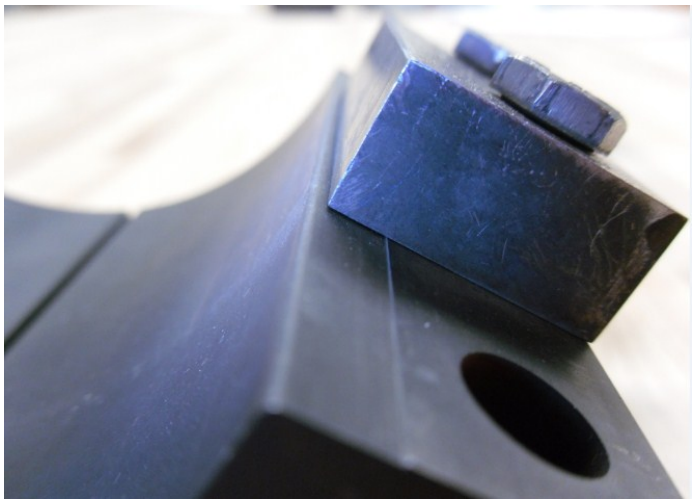

(b)

Figure 3.4 Top and Bottom Foil Forming Jig (a) complete forming jig and (b) bottom portion of forming jig showing top foil fixed end contour.

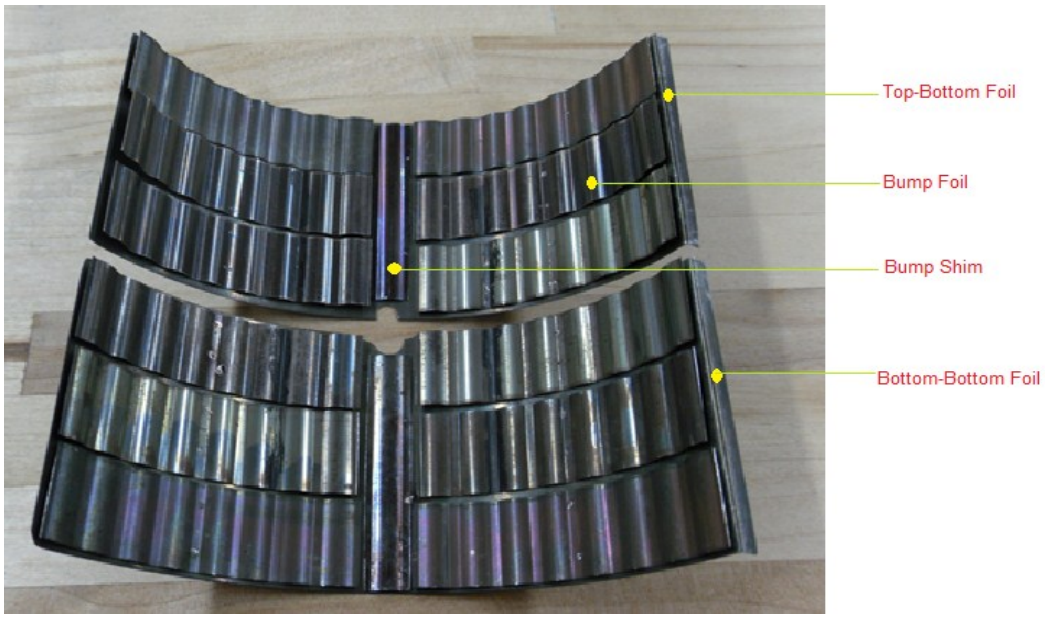

Figure 3.5 Manufactured Bottom Foil with Bump Foil.

Figure 3.6 Hydraulic Press for Cold Forming Process.

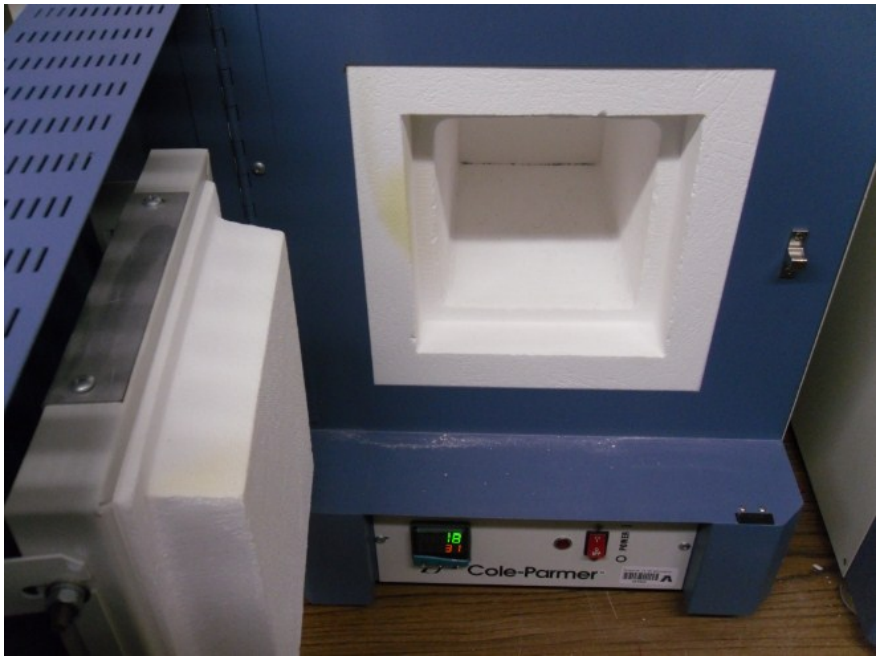

Figure 3.7 Electric Furnace for Foil Heat Treatment.

3.2.4 Corrugated bump foil

To improve rotor stability, corrugated bump foils are added beneath top foils to increase support stiffness and damping and hence improve load capacity. A picture of the bump foil forming jig made of Inconel 718 is shown in Figure 3.8. The same jig is used to manufacture both the 5 and 6 mils thick bump foils. The original HAFB design uses 6 mils thick bump foils/shims. Based on study presented in section 2.7, wear marks were found on edges of the bearing where higher temperature readings were also recorded. As a remedy, 5 mils thick bump foils are fabricated to replace 6 mils thick bump foils on the bearing edges. The original 6 mils thick bump foils were prefabricated and are made out of stainless steel 316. The 5 mils thick bump foils are constructed out of Inconel 750 assuming the two different materials exhibit similar material elastic property. The locations for spot welding of the bump foils/shims onto bottom foil are critical and they need to be chosen to allow the bump foil to stretch. Spot welding points are chosen on one side of the bump shims and at the center of the bump foils next to the yellow dots indicated in Figure 3.9. Undesired thermal bulges occur behind each spot weld point and their sizes are

significant compare to designed bearing clearance. Purging the backside of bottom foil after spot weld is vital to ensure bearing performance.

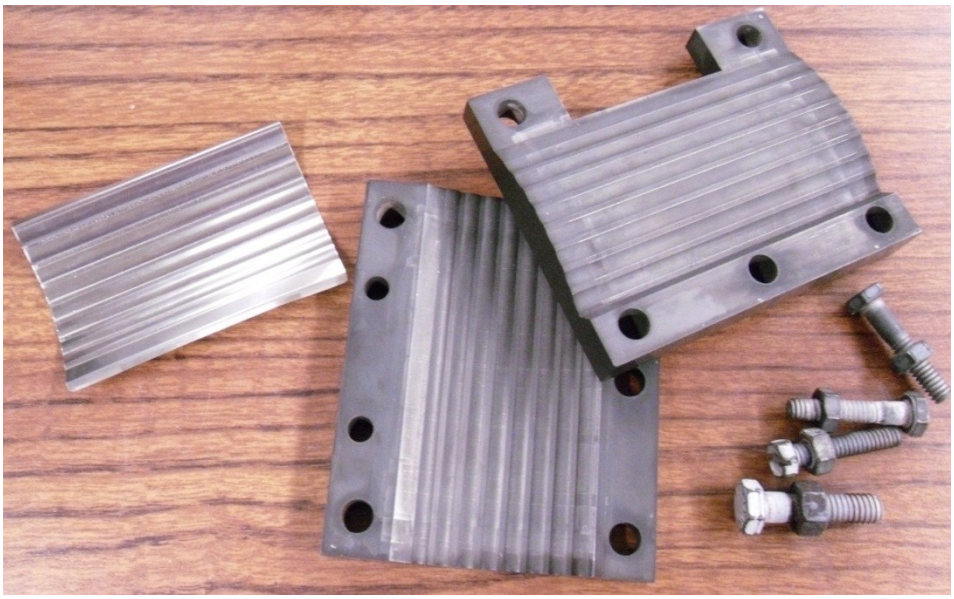

Figure 3.8 Bump Foil Forming Jig.

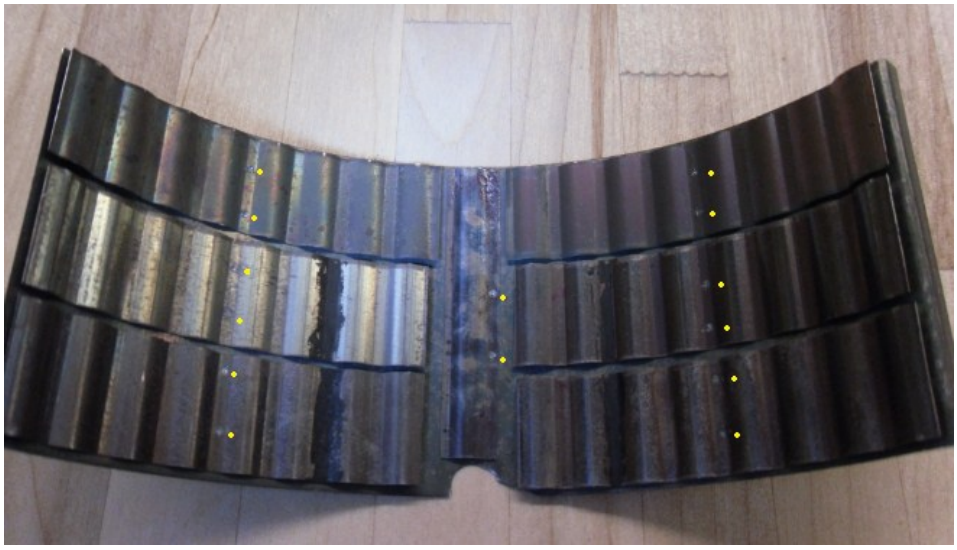

Figure 3.9 Spot Weld Location of Bump Foils.

3.2.5 Top foils

There are three top foils in the 3-pad configuration design for the hybrid air foil bearing. Each top foil is 6 mils thick and they are prefabricated prior to this research. For both top and bottom foil fabrication, the challenging part is to ensure the fixed end on each finishing part follows the edge contour shown in Figure 3.4 (b) as much as possible. Bearing static clearance for HAFB is very minuscule and limited so any nonconforming contour of the top and bottom foil can have significant effects on bearing performance. Rubbing marks due to manufacturing defects are inevitable under current manufacturing process, however they are acceptable considering the initial break-in during the previous 1000 start/stop endurance test, discussed earlier in Section 2.7, had smoothed out the top foil surface. Other rubbing marks around the air injection points are caused by another issue explained in detail in the next section. In addition, Teflon coatings are applied to each top foil on the contact surface as solid lubricant to alleviate concerns for dry rubbing at start/stop.

3.2.6 Orifice tubes

Orifice Tubes are made out of stainless steel 316 with 1.7 mm inner diameter and 2.1 mm outer diameter. The length of the orifice tube is not a specified measure though it is scaled long enough to reach beyond bearing sleeve for airline attachment. Figure 3.10 shows a solid model of the orifice tube with arrows indicating precautious regions during fabrication. Orifice tube is manually bent at arrow one with forming jig to ensure applied pressure is uniform and to eliminate undesired plastic deformation due to material ductility. This is done to guarantee unrestricted air flow passage around the corner. Grinding around the region indicated by the second arrow is required so the opening contour matches that on the back side of the top foil. The rubbing marks shown around the air injection point in were caused by thermal bulge created during laser welding of the orifice tube onto the top foil. This undesired thermal bulge is inevitable. However, this concern can be alleviated by grinding the orifice opening to match the contour on the backside of the top foil and hence reduce required effort during laser weld. Furthermore, there is interference

issue that needs to be address during the laser weld process. A holding mechanism was developed to hold the orifice tube at proper alignment with the top foil. A 3.175 mm wide opening gap is machined within the thickness of the bearing sleeve to compensate for orifice tubes and orifice tube should not intervene with the bearing sleeve. Incisions are marked on the backside of the top foil are shown in Figure 3.11 that function as guide during laser weld process. In addition, the length of the orifice tube should ideally be parallel with the top foil at side level view to also eliminate intervention with bearing holder when the bearing is assembled.

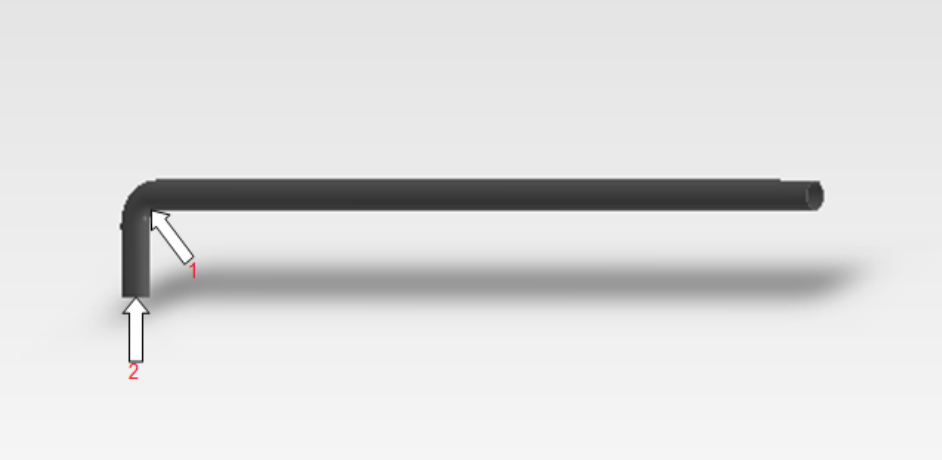

Figure 3.10 Solid Model of Orifice Tube.

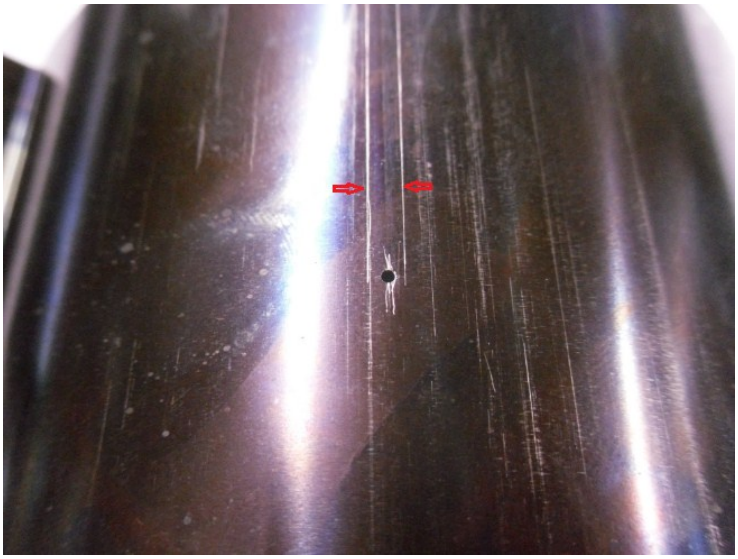

Figure 3.11 Incision Marks on Top Foil.

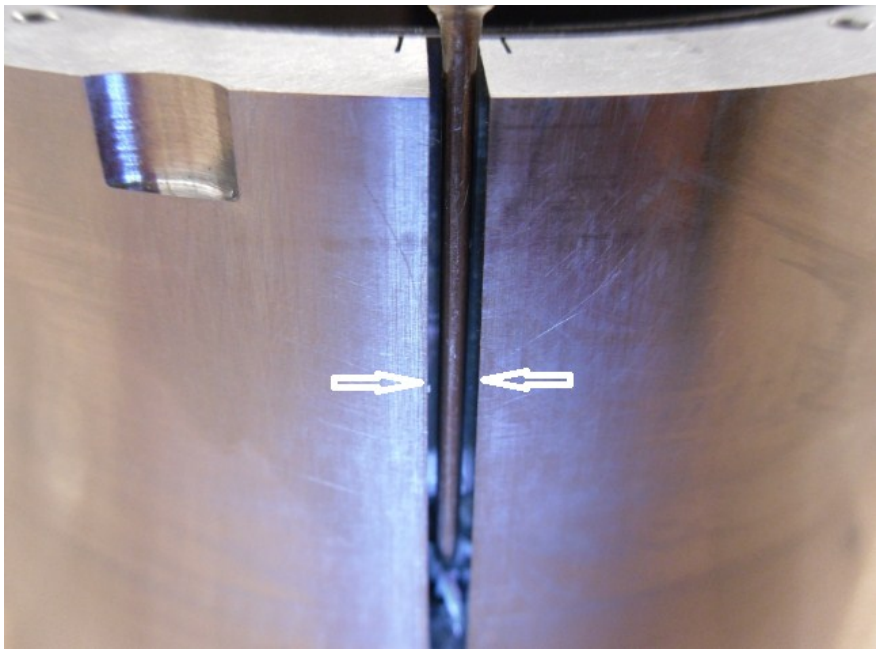

Figure 3.12 Orifice Tube Interference with Bearing Sleeve.

3.3 HAFB Assembly

There are a few cautions that need to be attended to during hybrid air foil bearing assembly. The bearing sleeve should be secured in both circumferential and axial direction. Figure 3.13 shows the front and back constraint mechanisms for blearing sleeve. Note the diameter of the constraint mechanism overlaps onto bearing sleeve hence prevents bearing sleeve form sliding in and out of the bearing holder.

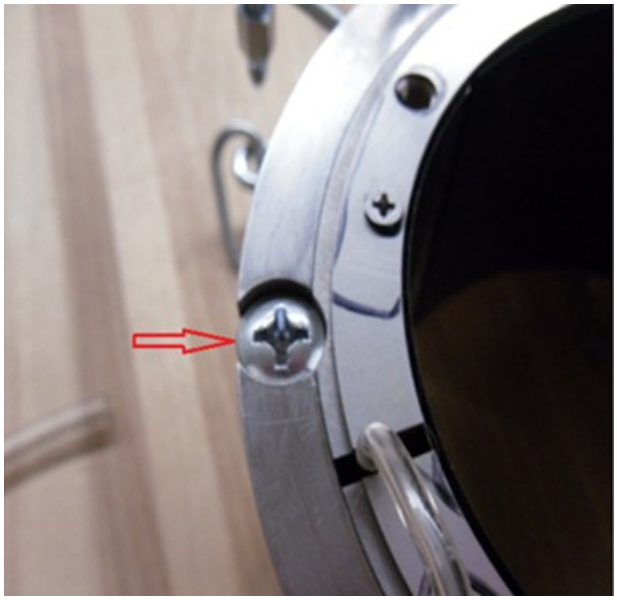

(a)

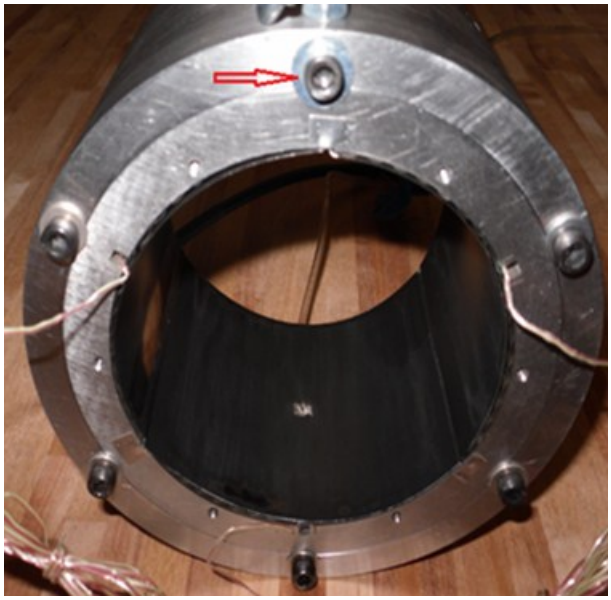

(b)

Figure 3.13 Bearing Sleeve Constraint Mechanism showing (a) HAFB assembly front end and (b) HAFB assembly rear end.

In order to monitor temperature, three thermal couples are bonded onto the bearing sleeve shown in Figure 3.14 and they are relayed out of the assembly through axial grooves that are contained beneath bottom foil as seen in Figure 3.15. It is critical to inspect for overlap underneath bottom foil.

In addition, it is important to confirm the bottom foil and top foil fixed ends sit properly into the accommodating fine slits. This can be done by moderately pressing on the foil while sliding down along the slits to make sure the contour of the foil at fixed end follow that on the bearing sleeve as indicated in Figure 3.16. Proper assemble is critical to avoid undesired buckle that impairs the bearing foundation.

Lastly, end plates are manufactured to be assembled on one edge of the bearing sleeve that function as constraint mechanism that restrict foil sliding motion in and out of the sleeve. For conventional purpose, bearing edge containing end plates will be referred to as front end of the bearing assembly. Three pieces of 5 mils thick squares are spot welded on the back end of the assembly covering slits opening on the opposing bearing edge. Figure 3.13 shows both front and back end of the complete assembly.

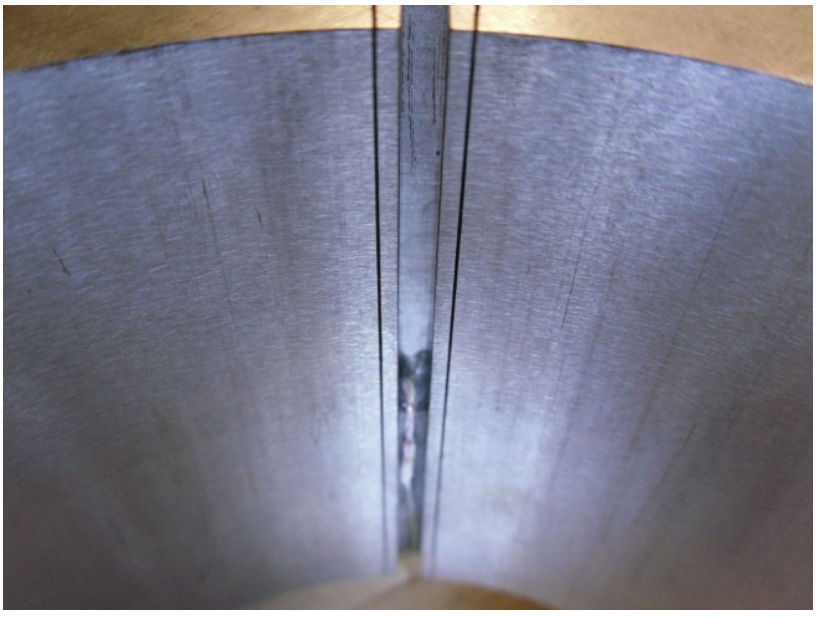

Figure 3.14 Thermal Couple Wire Attachment.

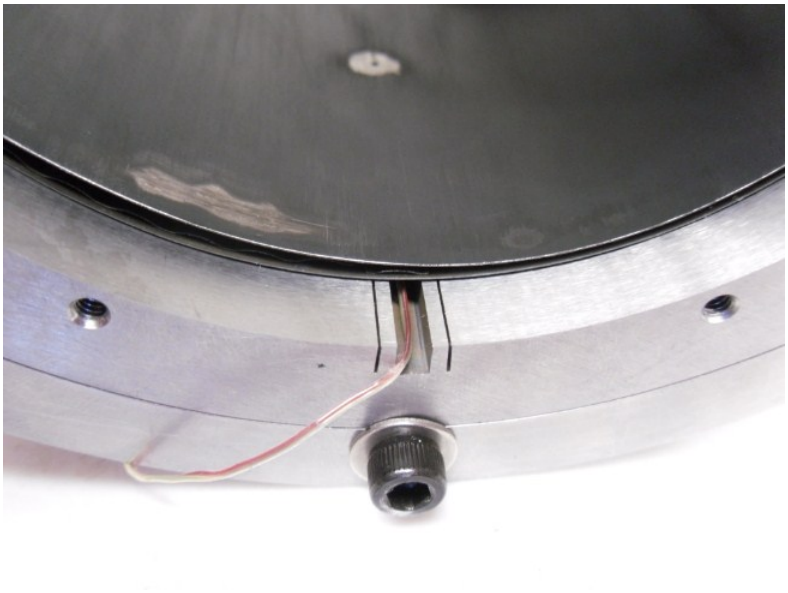

Figure 3.15 Thermal Couple Wire Relay.

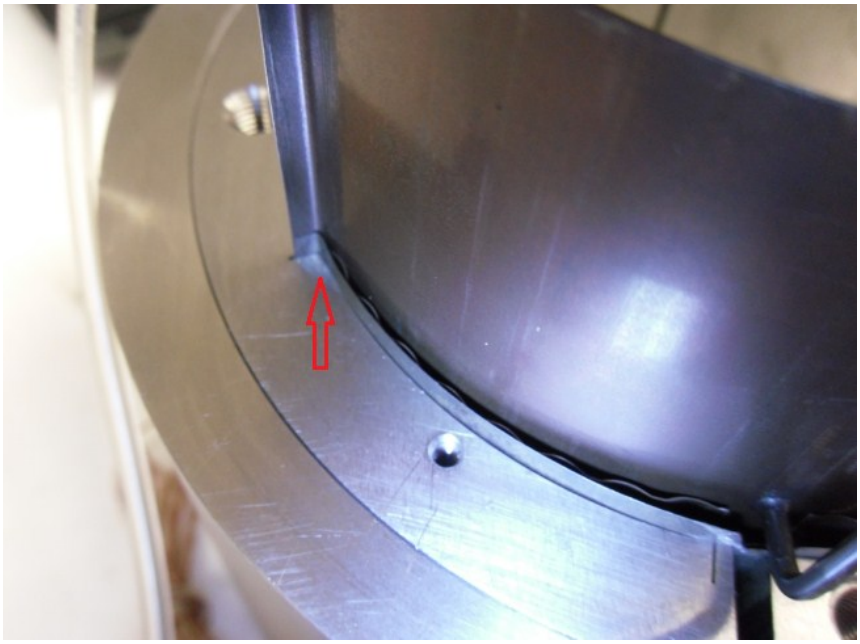

Figure 3.16 Top and Bottom Foil Assembly.

CHAPTER 4

IMPULSE EXCITATION TEST RIG

The test facility constructed previously for the start/stop endurance test presented in section 2.7 is used for the current thesis. The purpose of this research is to extract hybrid air foil bearing dynamic characteristics from bearing vibration response caused by impulse excitation using impact hammer. The test rig is constructed upon a heavy, vibration-free, and precision ground steel table to eliminate inertial effects contribution from the test rig foundation. A 40hp, 30,000 rpm motor provides stable shaft power. Rotor is connected to the motor through a flexible coupling to compensate for misalignments in axial, radial, and angular direction as well as to provide vibration damping and noise reduction. The rotor is driven by motor at one end and supported by duplex angular contact ball bearings. Hereinafter, the bearing end will be referred to as front end of the test rig and motor end will be referred to as back end of the test rig. Figure 4.1 shows picture of the complete test rig setup. Description of each numbered item is listed below.

1. Pressure Transducer Line: An Omegadyne PX409-100G5V pressure transducer is introduced into the system to monitor gage pressure within the bearing. It measures 0~100 gage pressure with 0~5 DC voltage output. It is connected to one of the four flow ports at the flow splitter. Bearing force coefficients are determined at various pressures from 30 to 60 psi.
2. Up Stream Pressure Regulator: For the purpose of this experiment, the upstream pressure regulator is employed as air flow valve. Air flow can be regulated here while monitoring the pressure transducer process meter for the desired pressure.
3. Pressure Transducer Process Meter: The process meter takes the output from the pressure transducer and converts it to display measured data in psi unit.

4. Flow Splitter: The air source flow is separated after the pressure regulator into four streams with the flow splitter. One port is connected to the pressure transducer and the other three are connected to each of the three orifice tubes.
5. Electric Motor: The 40hp motor is the power source of the test rig. Shaft power is transmitted through flexible coupling to the rotor.
6. External Load: Load is being applied through a pulley mechanism shown on top of the figure. It is then evenly distributed at two locations along the axis on the bearing holder in order to create access for impact hammer to strike at the center of the bearing assembly to avoid conical motion.
7. Duplex Ball Bearing Seal: The rotor is supported by two sets of duplex ball bearings on each side of the bearing assembly. Oil mist lubricant is circulated within the ball bearings from plastic tubing attached to the top of the seal and is then drawn out from the bottom of the seal and recycled back to the oil reservoir.
8. Electric Motor Cooling Line: The cooling oil is circulated through the motor then into a radiator to maintain temperature within the motor for sustained performance.
9. Torque Preload Line: This is connected to a 5lb. weight through pulley shown in top right corner of the figure. This is implemented into the rig for load cell installation.
10. Torque Rod: Installed onto the bearing holder on one end and connected to preload and load cell on the other, the torque rod functions as bearing friction force transmitter.
11. Load Cell: Load cell measures friction torque of the hybrid air foil bearing due to viscous shear generated within the air film. The friction force is transmitted through torque rod then picked up at the load cell.
12. Proximity Probe X: A pair of inductive type proximity probes (Bently Nevada P/N 330171-00-20-05-02-00) is installed on both the top and the side of the bearing holder to measure vibration response.

13. Proximity Probe Y: (see above)

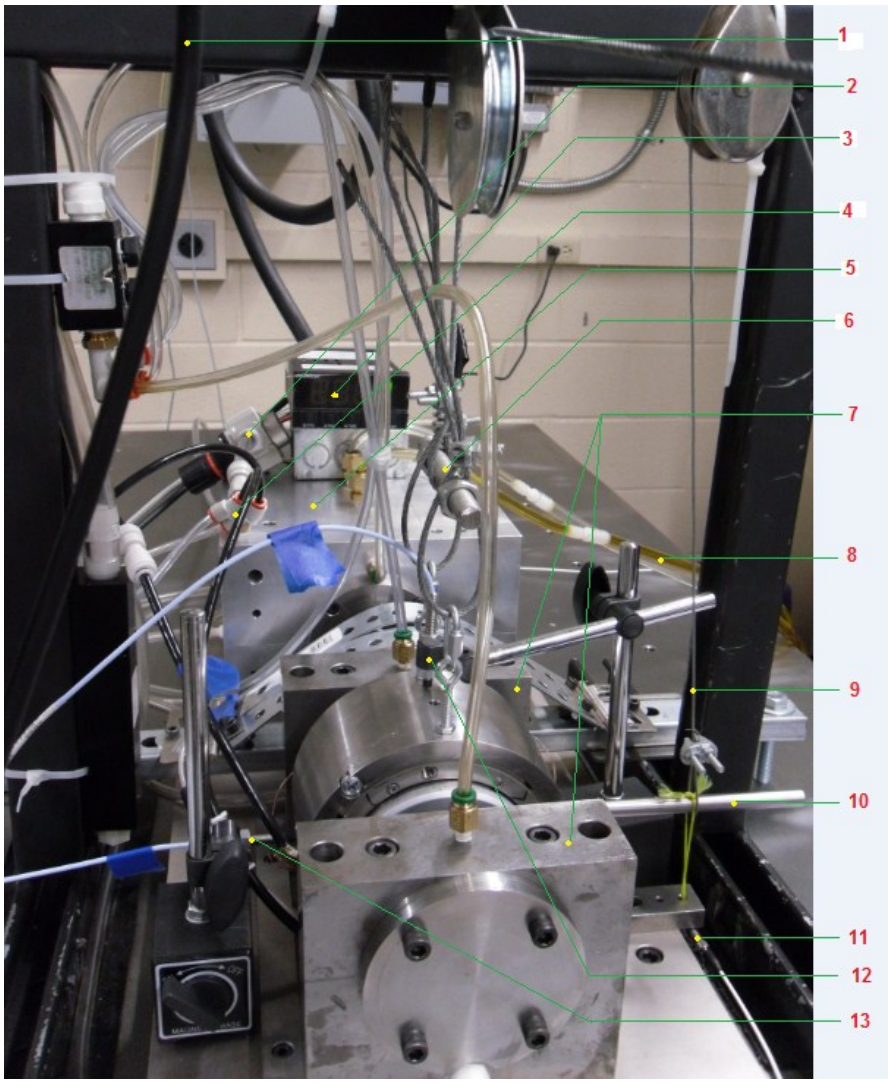

Figure 4.1 HAFB Test Rig.

4.1 Test rig set up

The orientation of the bearing is critically correlated to direction of the rotor spin as previously mentioned in Section 1.1.1. For a counter-clockwise rotor spin viewed from the bearing perspective, the front end of the bearing must match the front end of the test rig so the rotor spins from fixed end of one top foil to free end of another top foil as displayed in Figure 4.3. The external load is being applied through a pulley mechanism hanging over the bearing and

extended beyond the edge of the test bed. The three-pad HAFB is assembled for a load-on-pad configuration and thus the 6 o'clock pad is loaded as shown in Figure 4.4. There is an opening notch on top of the ball bearing that should be aligned to plastic tubes feeding oil mist lubricant and it is critical to check for alignment when installing ball bearing seal as shown in Figure 4.5.

It is important to differentiate the operating fundamentals between physical hybrid air foil bearing application and how the test apparatus is built for the purpose of this research. In a physical application, the bearing is being held fixed and the rotor should be free to vibrate in response to applied load and disturbances. In the test rig, the rotor is being held fixed by two sets of duplex ball bearings on each side of the free-hanging hybrid air foil bearing. The motor power is transmitted through a flexible coupling to assure only torque is being transmitted to spin the rotor. Nevertheless, the nature of the bearing dynamic characteristics is equivalent in both cases. In another word, the rigid rotor is assumed to be fixed while the HAFB is allowed to vibrate in response to excitation and stiffness and damping coefficients are identical in both cases. HAFB reference frame is defined in Figure 4.2 for the bearing-rotor system. In the current experimental set up, impulse excitations are applied in the positive X and negative Y directions by striking the top and left side of the bearing assembly with respect to front view.

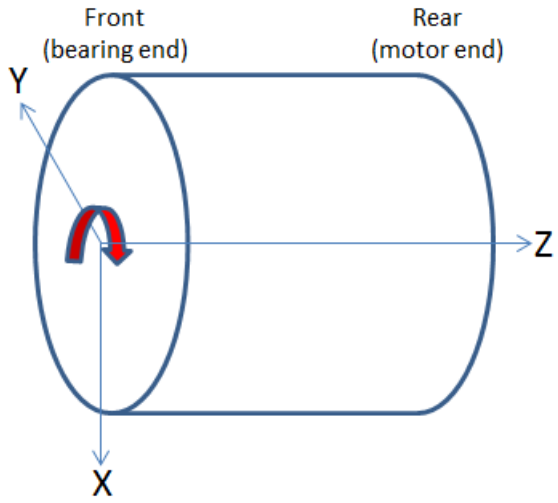

Figure 4.2 HAFB Reference Frame.

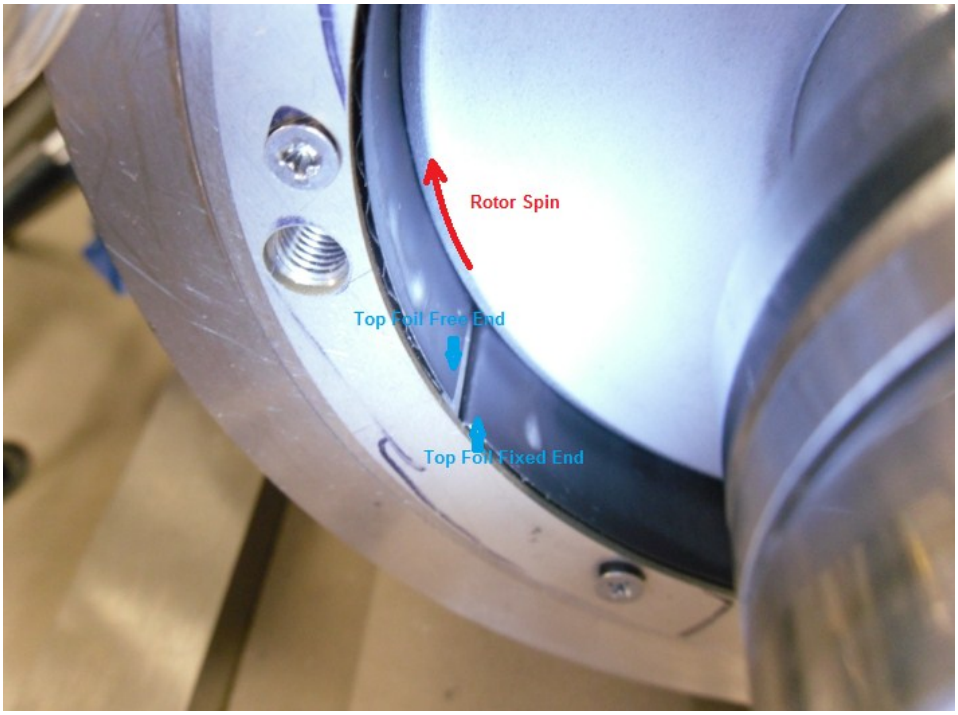

Figure 4.3 HAFB Orientation With Respect to Rotor Spin.

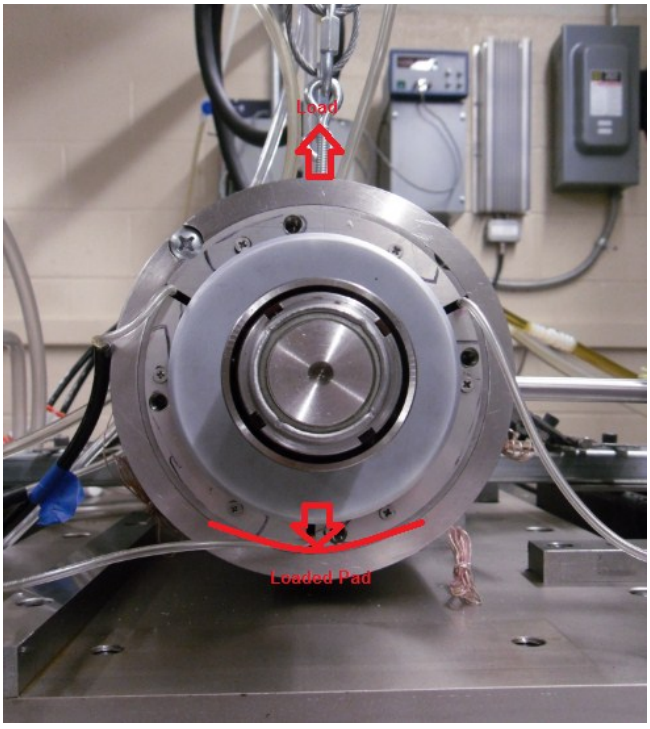

Figure 4.4 Applied Load and Loaded Pad.

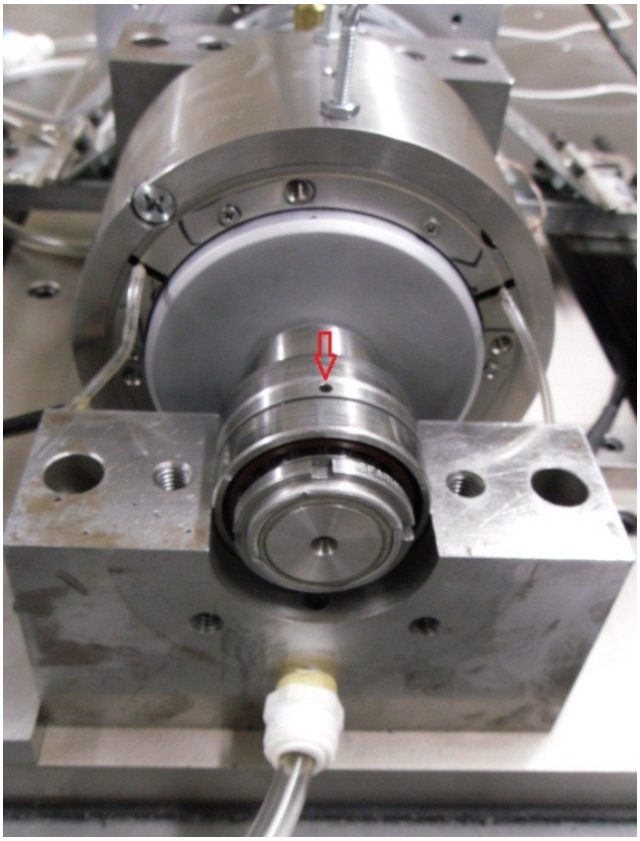

Figure 4.5 Oil Mist Lubricant Access Alignment.

4.2 Measuring devices and data acquisition set up

The inductive type proximity probes are sensitive to surface material and calibration is required for more accurate measurements. The DC voltage output from proximity probes are calibrated with respect to 50 μm increments up to 800 μm. Figure 4.6 represents proximity probes calibration curve. Note that the nonlinear portion for proximity less than 50 μm is neglected. Proximity probes used in this research has manufacturer-specified range up to 10V and they are installed with roughly 200~300 μm offset from the bearing holder surface.

PCB impact hammer 086C02 is used for this experiment as bearing excitation source. Built in force sensor is mounted on the striking end of the hammer head which can be installed with variety of impact tips that transmit impact force to the sensor. It is recommended to use stiffer tip

for this experiment due to the nature of high frequency response characteristics of the test subject. The impact hammer shown in Figure 4.7 is connected to data acquisition system through a PCB 482A16 signal conditioner providing constant current source under 20 mA. Manufacturer provided sensitivity rating is 50 mV/lbf.

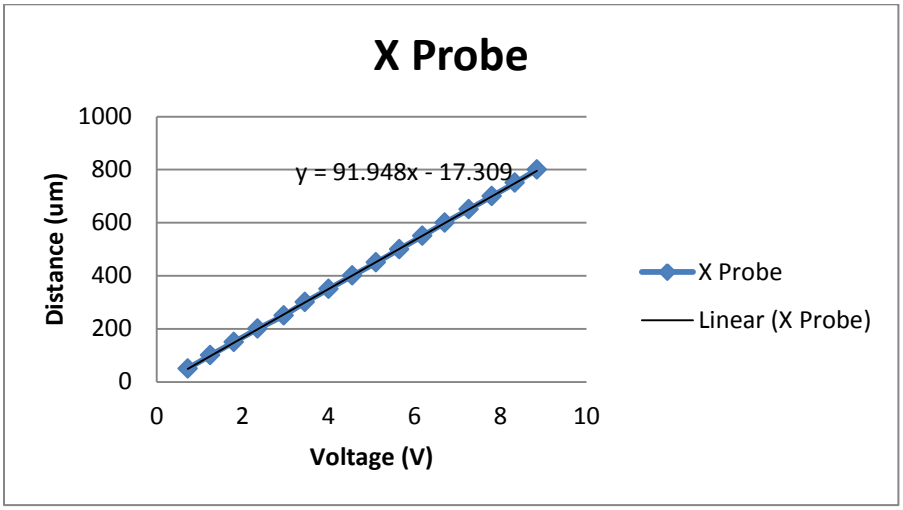

(a)

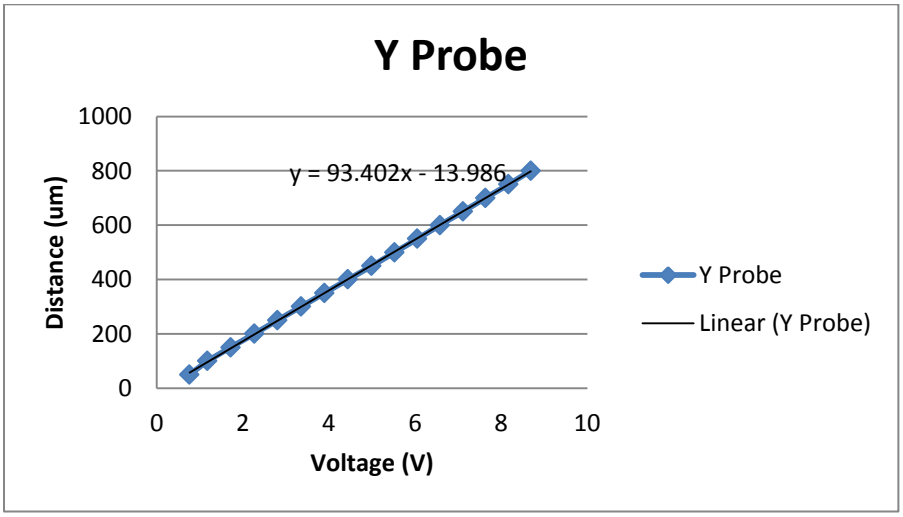

(b)

Figure 4.6 Proximity Probe Calibration Curve for (a) vertical proximity sensor and (b) horizontal proximity sensor.

Figure 4.7 PCB Impact Hammer.

PCI 4722 dynamic signal acquisition board from National Instruments is used for the experiments for the high frequency vibration of the hybrid air foil bearing impulse response. Proximity probes signals collected from bearing vibration response are processed with LabVIEW built-in low pass filter to remove electronic noise inherent within the measurements. Additional data process is crucial to eliminate system baseline signal due to rotor imbalance at non-zero speed for bearing force coefficients identification. Impulse response acquired from the proximity probe includes vibration due to imbalance generated from existing uneven friction and manufacture flaws within the mechanical structure. For that reason, passive data collection is manually activated for baseline signal measurements and passive aggressive data collection is triggered at each incident during initial excitation input for impulse response measurements. Detail description of the data acquisition file is included in the appendix. The baseline subtraction procedure to eliminate baseline signals will be presented in the following chapter.

CHAPTER 5

METHODOLOGY

5.1 Least square method for identification of bearing characteristics

In experimental practice, bearing stiffness and damping coefficients estimation techniques have been proposed both in time-domain and frequency-domain. However, bearing parameter identification in time-domain requires numerical differentiation of the measured vibration signal to determine velocity and acceleration components of journal motion. This produces biased error due to intrinsic noise presented in the measured data. In addition, the accuracy of the time-domain estimation depends on the number of sets of linearly independent data across a wide range of frequency spectrum. Researchers suggested that bearing force coefficients identification in the frequency-domain with impact excitation method is therefore more efficient and practical (9-11). Methodology introduced in this research was developed by Qiu and Tieu (10) to determine two journal bearing coefficients from the transfer functions of the displacement to the excitation force using least square estimation.

For a simple one degree of freedom damped system, the equation of motion is expressed as equation(9). The equation can be manipulated using Laplace transform and Euler's equation to obtain equation (10), (11), and (12) Knowing vibration response, force input and mass property, the spring constant as well as damping can be determined by separating the real and imaginary part of equation (12)

$$m\ddot{\quad} \quad \cdot \quad f(t) \tag{9}$$

$$m(j\omega)^2 X(s) + d(j\omega)X(s) + kX(s) = F(s) \tag{10}$$

$$[(k-m\omega^2)+d(j\omega)]X_0 e^{j\phi_x} = F_0 e^{j\phi_F} \tag{11}$$

$$[(k-m\omega^2)+d(j\omega)]X_0(\cos\phi_x + j\sin\phi_x) = F_0(\cos\phi_F + j\sin\phi_F) \tag{12}$$

5.2 Least square method for 2DOF system

Equations of motions for the 2DOF rotordynamics system (Figure 5.1) are presented below. In this study, vibration signals (X and Y) and excitation forces ($f_x(t)$ and$f_y(t)$) are measured quantities and the application of least square method allow identification for system stiffness, damping, and mass properties as unknown in equation(13).

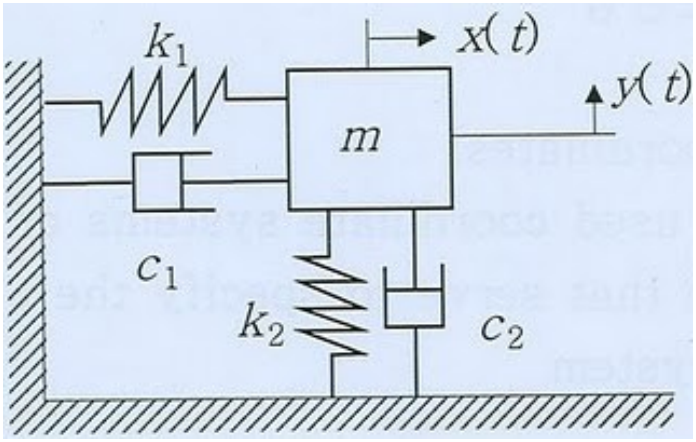

Figure 5.1 2DOF mass spring damper system.

$$m\ddot{} \qquad \cdot \qquad \cdot$$
$$m\ddot{} \qquad \cdot \qquad \cdot \tag{13}$$

By taking Laplace transform of equation(13) and rearrange:

$$\begin{aligned} -m_{xx}\omega^2 X_x - m_{xy}\omega^2 X_y + k_{xx}X_x + d_{xx}j\omega X_x + k_{xy}X_y + d_{xy}j\omega X_y &= F_x \\ -m_{yy}\omega^2 Y_y - m_{yx}\omega^2 Y_x + k_{yy}Y_y + d_{yy}j\omega Y_y + k_{yx}Y_x + d_{yx}j\omega Y_x &= F_y \end{aligned} \tag{14}$$

In matrix form:

$$\begin{bmatrix} k_{xx} - m_{xx}\omega^2 + d_{xx}j\omega & k_{xy} - m_{xy}\omega^2 + d_{xy}j\omega \\ k_{yx} - m_{yx}\omega^2 + d_{yx}j\omega & k_{yy} - m_{yy}\omega^2 + d_{yy}j\omega \end{bmatrix} \bullet \begin{bmatrix} X & X \\ \cdots_x & \cdots_y \end{bmatrix} = \begin{bmatrix} F_x & 0 \\ 0 & F_y \end{bmatrix} \quad (15)$$

Where the first term of equation (15) defined for system impedance can be further divided to factor out system stiffness, mass, and damping properties:

$$\begin{bmatrix} k_{xx} - m_{xx}\omega^2 + d_{xx}j\omega & k_{xy} - m_{xy}\omega^2 + d_{xy}j\omega \\ k_{yx} - m_{yx}\omega^2 + d_{yx}j\omega & k_{yy} - m_{yy}\omega^2 + d_{yy}j\omega \end{bmatrix} = \begin{bmatrix} 1 & 0 & -\omega^2 & 0 & j\omega & 0 \\ 0 & 1 & 0 & -\omega^2 & 0 & j\omega \end{bmatrix} \bullet \begin{bmatrix} k_{xx} & k_{xy} \\ k_{yx} & k_{yy} \\ \cdots & \cdots_y \\ \cdots_{yx} & \cdots_{yy} \\ d_{xx} & d_{xy} \\ d_{yx} & d_{yy} \end{bmatrix} \quad (16)$$

The least square method utilized to solve the system's stiffness and damping requires data collection at different frequencies and Fourier transform enables the ability to generate frequency sweep data of the measured vibration signal with one impulse input. Let matrix D be formulated by Fourier transform of the measured vibration responses (X and Y) and matrix $\hat{F}$ be formulated by Fourier transform of the forcing function ($f_x(t)$ and$f_y(t)$). Then equation (15) can be represented as equation (17) and the measured impedances matrix H at each frequency (index i), can be defined as equation(18). Comparing equation (17) with equation(15), it can be observed that matrix H contains the system stiffness, mass, and damping properties that are factored out in equation(16).

$$\begin{pmatrix} H_{xx_i} & H_{xy_i} \\ H_{yx_i} & H_{yy_i} \end{pmatrix} \cdot \begin{pmatrix} D_{xx_i} & D_{xy_i} \\ D_{yx_i} & D_{yy_i} \end{pmatrix} = \begin{pmatrix} F_{x_i} & 0 \\ 0 & F_{y_i} \end{pmatrix} \quad (17)$$

$$\begin{pmatrix} H_{xx_i} & H_{xy_i} \\ H_{yx_i} & H_{yy_i} \end{pmatrix} = \begin{pmatrix} F_{x_i} & 0 \\ 0 & F_{y_i} \end{pmatrix} \cdot \begin{pmatrix} D_{xx_i} & D_{xy_i} \\ D_{yx_i} & D_{yy_i} \end{pmatrix}^{-1} \tag{18}$$

The first subscripts represents corresponding system properties and measured quantities in x and y direction and the second subscripts represents bearing response in the x and y direction. By taking inverse of the impedance matrix, the system measured flexibility matrix F can be found by taking inverse of right hand side of equation(18).

$$F = \begin{pmatrix} F_{xx_i} & F_{xy_i} \\ F_{yx_i} & F_{yy_i} \end{pmatrix} = \begin{pmatrix} H_{xx_i} & H_{xy_i} \\ H_{yx_i} & H_{yy_i} \end{pmatrix}^{-1} = \left(\begin{pmatrix} F_{x_i} & 0 \\ 0 & F_{y_i} \end{pmatrix} \cdot \begin{pmatrix} D_{xx_i} & D_{xy_i} \\ D_{yx_i} & D_{yy_i} \end{pmatrix}^{-1} \right)^{-1} \tag{19}$$

Least square method can be applied to equation (19) to formulate equation (20) where F represents the measured flexibilities, H the approximated unknown impedances to be identified, I the identity matrix, and E the error to be minimized. Recall system impedance (matrix H) representation in equation(16). Rearranging equation(20), the system property can then be solved using multivariable regression. The A matrix in left hand side of equation (21) is formed by stacking the decomposed real and imaginary parts alternatively for each frequency as expressed in equation(22) where F_i components correspond to measured system flexibility at each frequency component. In this case, let the number of frequencies be 150 to divide frequency sweep. The size of A matrix becomes 600×6 and the size of I matrix becomes 600×2.

$$F \cdot H = I + E \tag{20}$$

$$A \cdot \begin{pmatrix} k_{xx} & k_{xy} \\ k_{yx} & k_{yy} \\ m_{xx} & m_{xy} \\ m_{yx} & m_{yy} \\ c_{xx} & c_{xy} \\ c_{yx} & c_{yy} \end{pmatrix} = I + E \tag{21}$$

$$\begin{aligned} &\mathrm{Re}\left[F_i \cdot \begin{bmatrix} 1 & 0 & -(\omega_i)^2 & 0 & i \cdot \omega_i & 0 \\ 0 & 1 & 0 & -(\omega_i)^2 & 0 & i \cdot \omega_i \end{bmatrix} \right] \\ &\mathrm{Im}\left[F_i \cdot \begin{bmatrix} 1 & 0 & -(\omega_i)^2 & 0 & i \cdot \omega_i & 0 \\ 0 & 1 & 0 & -(\omega_i)^2 & 0 & i \cdot \omega_i \end{bmatrix} \right] \end{aligned} \tag{22}$$

5.3 Application of least square method on 2DOF simulated vibration signal

Practice of this methodology was performed on a two degree of freedom system. Simulated vibration response was generated with known bearing properties including cross coupling. The stiffness and damping of the system are tabulated in Table 5.1 to be compared with the results using least square method. The external force was generated to mimic impulse input allowing Fourier transform of the forcing function. The vibration response due to external force in x and y directions are plotted in Figure 5.2 and Figure 5.3.

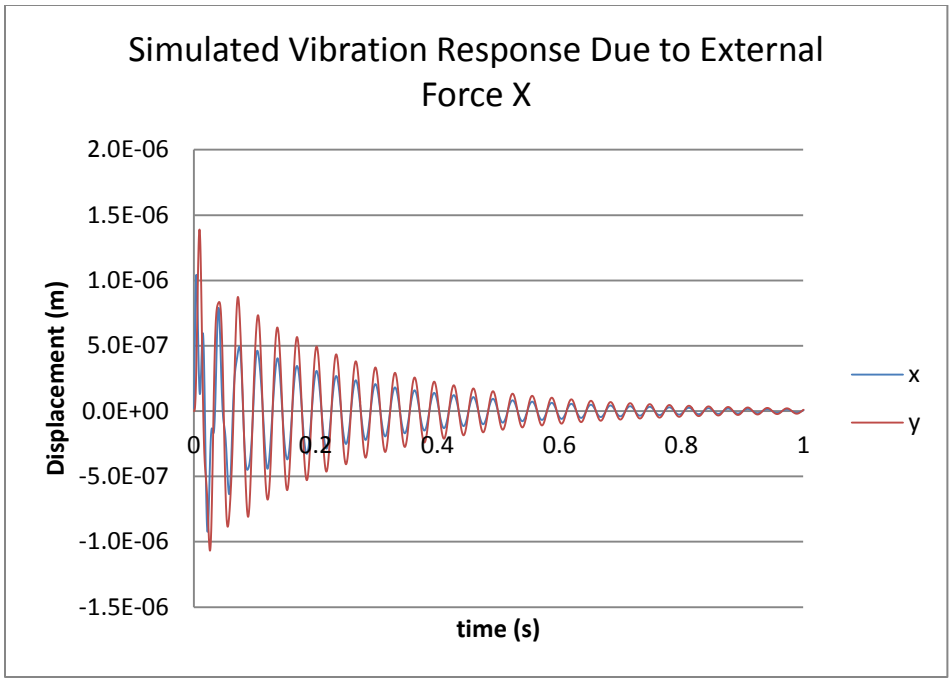

Figure 5.2 Vibration response of 2DOF system due to external force applied in x-direction.

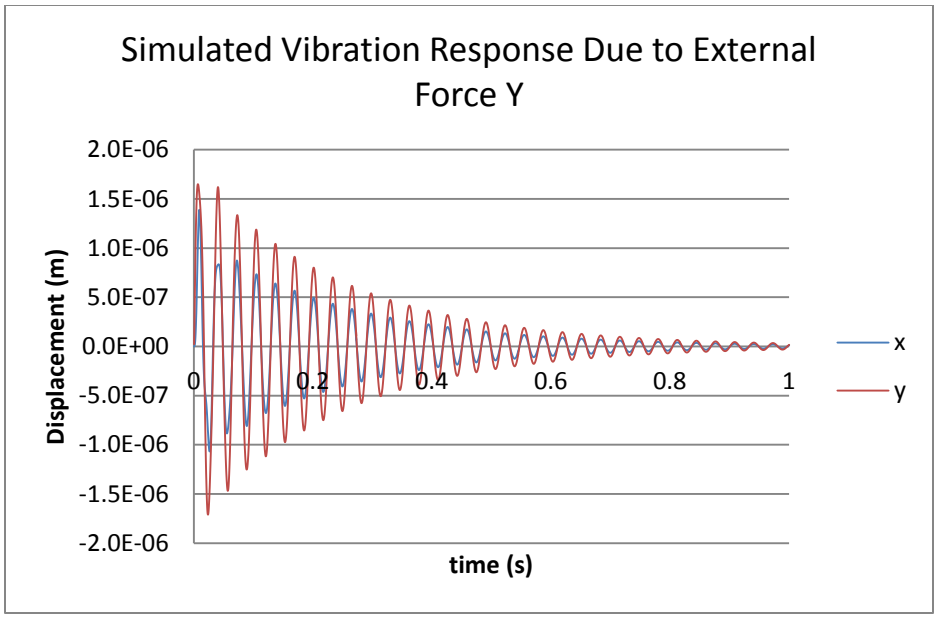

Figure 5.3 Vibration response of 2DOF system due to external force applied in y-direction.

It does not require a wide range of frequency sweep but in order to ensure more accurate results, frequency sweep needs to be done including the natural frequencies of the system. Stiffness and Damping coefficients are tabulated below (Table 5.2 to Table 5.4) to compare results with different range of frequency sweep. Amplitude of the system's flexibility is plotted in Figure 5.4 to help determine the range of frequency sweep. The resulting stiffness-mass-damping matrix from least square method has size 6×2 and they are tabulated in Table 5.1.

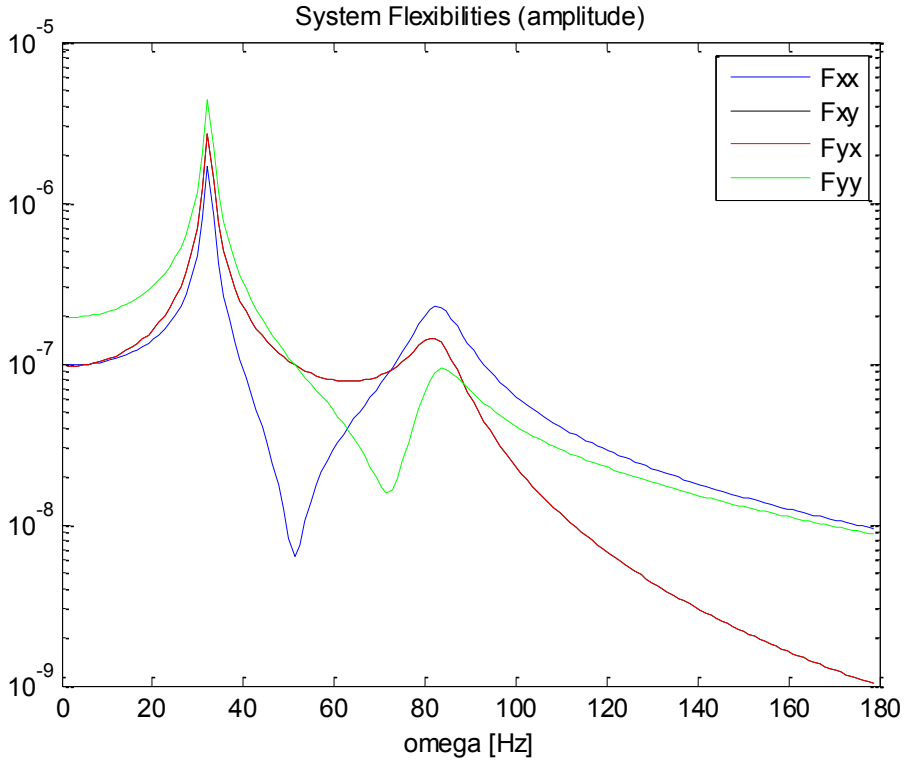

Figure 5.4 Amplitude plot of 2DOF system.

Table 5.1 Least square method stiffness, mass and damping of 2DOF system

Simulation Property		Least Square Method Property	
k_{xx}=2E+7	k_{xy}=-1E+7	k_{xx}=1.98E+7	k_{xy}=-9.74E6
k_{yx}=-1E+7	k_{yy}=1E+7	k_{yx}=-9.74E+6	k_{yy}=1.00E+7
m_{xx}=100	m_{xy}=0	m_{xx}=94.096	m_{xy}=1.8308
m_{yx}=0	m_{yy}=100	m_{yx}=1.8252	m_{yy}=95.947
d_{xx}=4.5E+3	d_{xy}=-2.5E+3	d_{xx}=5.2916E+3	d_{xy}=-2.8886E+3
d_{yx}=-2.5E+3	d_{yy}=2.5E+3	d_{yx}=-2.8868E+3	d_{yy}=2.8805E+3

Table 5.2 Frequency range 50 Hz to 80 Hz

k_{xx}=2.00E+7	k_{xy}=-9.97E+6
k_{yx}=-9.84E+6	k_{yy}=1.00E+7
m_{xx}=95.662	m_{xy}=1.4449
m_{yx}=1.9926	m_{yy}=96.814
d_{xx}=5746.5	d_{xy}=-23.315
d_{yx}=-26.661	d_{yy}=6220.2

Table 5.3 Frequency range 20 Hz to 60 Hz

k_{xx}=2.02E+7	k_{xy}=-9.97E+6
k_{yx}=-9.94E+6	k_{yy}=1.02E+7
m_{xx}=96.292	m_{xy}=1.3328
m_{yx}=1.5905	m_{yy}=97.906
d_{xx}=1225	d_{xy}=-439.77
d_{yx}=-440.32	d_{yy}=1266.6

Table 5.4 Frequency range 120 Hz to 160 Hz

k_{xx} =1.38E+7	k_{xy} =-1.01E+7
k_{yx} =-1.00E+7	k_{yy} =3.72E+6
m_{xx} =85.689	m_{xy} =1.3139
m_{yx} =1.3739	m_{yy} =86.861
d_{xx} =33040	d_{xy} =-2127.3
d_{yx} =-2127.3	d_{yy} =31435

5.4 General experimental approach

It is critical to check that the electric motor cooling and lubrication systems are both operating properly before running the motor. The motor control is implemented using Sieb & Meyer fcontrol8x 1.3 professional software. In addition to speed control, motor power output can be monitored in relation to existing friction generated due to either dry-rubbing between the top foil and the rotor or viscous shear within the air film. A checklist of conducting procedures for the experiment is presented below. Vibration signals are recorded after rotor reaches steady state.

- Lubrication
  - ✓ Check for valve openings in lubrication supply line
  - ✓ Check for valve openings in lubrication vacuum suction line
  - ✓ Power on oil mist generator
  - ✓ Turn on pressurized air supply and adjust lubrication supply pressure regulator
  - ✓ Monitor oil mist lubricant flow

- Motor
  - ✓ Power on motor cooling circulation
  - ✓ Power on motor cooling fluid cooling fan
  - ✓ Power on and adjust motor control power supply to 24 VDC
  - ✓ Switch on electric motor power AC power supply

- ✓ Establish motor control communication link

- Data Acquisition
  - ✓ Revise LabVIEW built-in low pass filter cutoff frequency with corresponding commended motor speed
  - ✓ Check for correct load cell gain for friction torque measurements in LabVIEW front panel
  - ✓ Check for correct impulse excitation trigger threshold for impulse response data collection
  - ✓ Monitor proximity probe signal and ensure vibration response oscillates within proximity probe linear range
  - ✓ Power on impact hammer signal conditioner/power supply and adjust signal gain
  - ✓ Check data save file path

Impulse response vibration signals are collected for excitations both in the vertical (X) and horizontal (Y) directions. For each excitation, vibration response picked up from the vertical and horizontal proximity probes as well as impact force are recorded at 10k Hz sampling rate with respect to 0.0001 seconds time increments.

Vibration response recorded at non-zero rotor speed contains baseline signals due to rotor imbalance in addition to response due to excitation. Baseline subtraction is necessary to eliminate baseline signals in order to identify bearing force coefficients. It can be observed that vibration due to rotor imbalance is synchronous with the rotor spin speed as presented in Figure 5.5. Tachometer signals are registered at each rotor spin revolution and baseline signals exhibits one cycle for each of the horizontal and vertical vibration per rotor revolution.

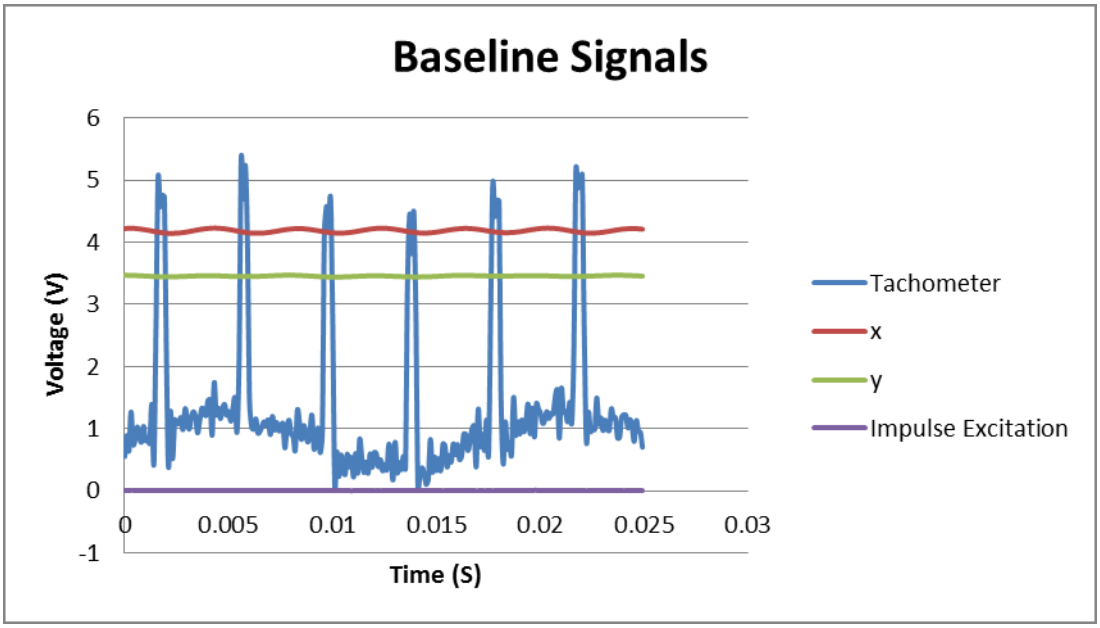

Figure 5.5 HAFB Baseline Signals at 15000 RPM.

Two sets of proximity probe measurements are required for baseline subtraction: one for baseline signals due to rotor imbalance and one for impulse response. From the impulse response, time delay between each tachometer signal and impulse excitation signal can be determined. Since baseline signals is synchronous with tachometer signal, the time delay between the tachometer signal and impulse excitation can be directly translated into phase lag of impulse response in relation to synchronous baseline signals. Another word, in order to extract vibration due to pure impulse excitation, baseline signal is subtracted from impulse response with respective time delay between each impulse excitation and tachometer signal.

For demonstration, impulse response is presented in Figure 5.6 indicating phase lag between tachometer signal and impulse excitation at 15000 rpm supplying 60 psi hydrostatic pressure. Measured impulse response shown in Figure 5.6 also contains vibration due to imbalance and hence, vibration signals with corresponding phase lag from baseline signal data are subtracted from the impulse response.

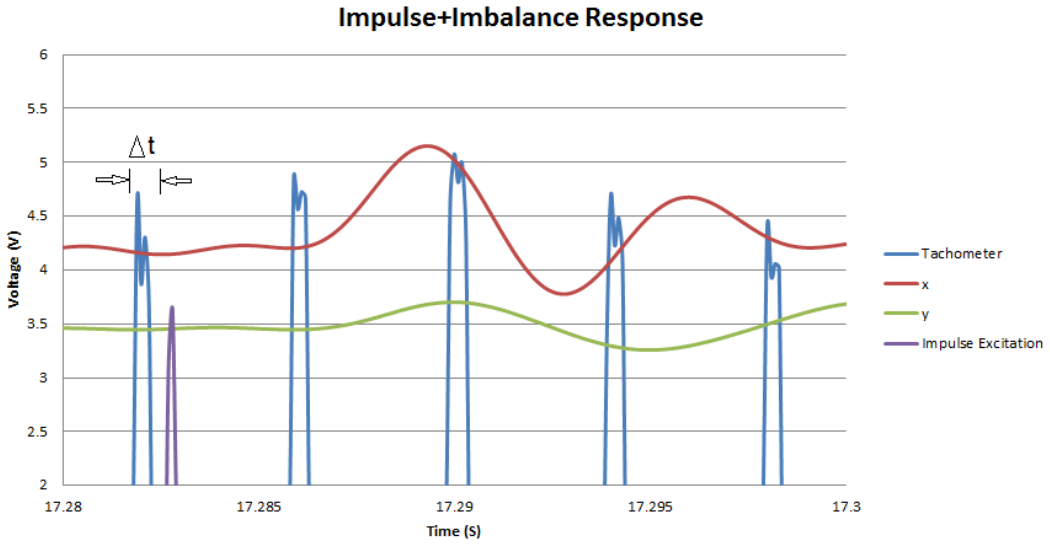

Figure 5.6 HAFB Impulse Response at 15000 RPM.

5.5 Modification to experimental procedure

5.5.1 PCB Impact Hammer

The original impact hammer purchased has linear sensitivity curve of 11.2 mV/N up to a measurement range of ±444 N. The magnitude of the resulting impulse response is comparably similar to those of residual noise presented in the impulse response data after signal process. Therefore, the impulse response data could not be used to deliver reliable identification of the bearing force coefficients. Calibration of 086C02 impact hammer was carried out in the lab to confirm factory provided sensitivity curve. Subsequently, 086C02 was replaced by 086C03 impact hammer which has linear sensitivity curve of 2.24 mV/N up to a measurement range of ±2224 N.

5.5.2 Signal Process

It was brought to attention the impact of digital filter on collected response data. There are both magnitude and phase distortion on the filtered signal compare to ideal signal. In the original signal process scheme, vibration signals are passed through the low pass filter previous to baseline subtraction. However, the impulse excitation input contains numerous unknown components of frequencies and should not be passed through the filter. As a result, the phase lag

between tachometer signal and filtered impulse response is now compromised and contains the original phase lag plus an unknown phase distortion due to signal process with digital filter. The concept of baseline subtraction is established upon the assumption that phase lag between tachometer signal and impulse excitation is the same as that between tachometer signal and impulse response. Consequently, the original signal process scheme is modified to perform baseline subtraction before passing the impulse response data through lowpass filter.

A MATLAB code is created for signal processing including baseline subtraction. The program takes the time continuous raw vibration response collected using LabVIEW, identifies phase lags between tachometer signals and impulse excitations, separates each impulse response for baseline subtraction, and then stores the data after further signal process within a lowpass filter subroutine. The digital filter is constructed using 4^{th} order Chebyshev filter function with cutoff frequency chosen slightly above respective rotor operating speed. Figure 5.7 presents a general schematic description of the data process procedure.

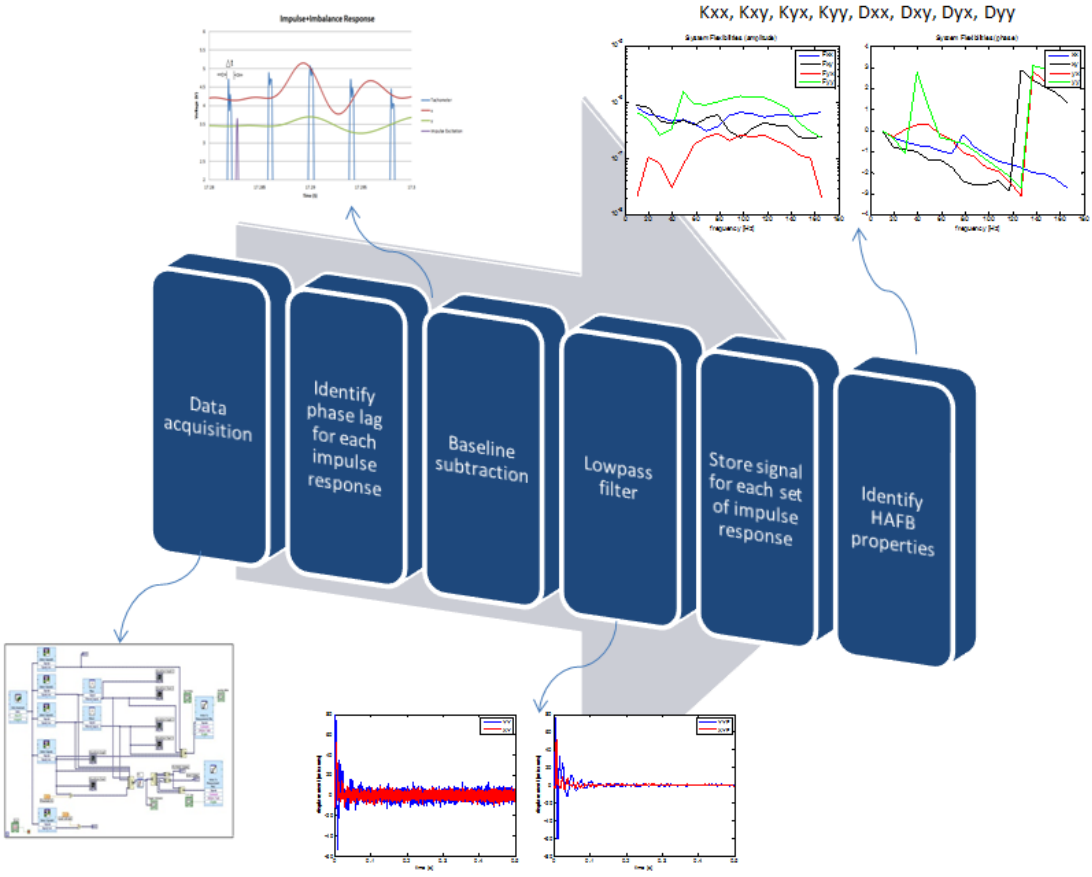

Figure 5.7 Data Process Scheme.

5.5.3 Bearing Assembly Axial Constraints

At the tested speeds of 12k, 15k, and 18k rpm, friction between the hybrid air foil bearing and the rotor is very miniscule and the combining effects of hydrostatic and hydrodynamic operation enables the bearing assembly to slide in the axial direction when excited by impulse excitation. Vibration response is measured by proximity probes slightly offset from the bearing holder surface which cannot be assumed to be uniformly even. Up to 50 microns of circumferential changes in proximity was measured at one point when bearing assembly displaces in the axial direction. To remedy this issue, two additional air lines supplying hydrostatic pressure are held on each edge of the bearing assembly to restrict axial motion and improve the accuracy of the proximity probe measurements.

CHAPTER 6

RESULTS AND DISCUSION

6.1 Purposes of the experiments

The objective of this research is to utilize least square method to identify hybrid air foil bearing stiffness and damping coefficients from measured vibration signal when the bearing is excited with an impulse input using impact hammer. The sampling rate of the measurements is chosen at 10,000 Hz which is significantly above the frequency at which the bearing vibrates. Dynamic bearing force coefficients are measured under nine operating conditions; rotors speed of 12k, 15k, and 18k rpm as well as supplied air pressure at 50, 60, and 70 psi. The determined force coefficients are then plugged into rotordynamics code for analysis in the simulated environment. Comparisons of the magnitude and phase plots between measured and simulated vibration were performed to confirm experimental results.

6.2 Dynamic bearing force coefficients

Based on research results indicated in section 2.7, endurance tests were safely conducted for a fairly identical bearing at 8000 rpm under 445 N external load over five hours. Temperature fluctuations were monitored at different supplied air pressure for the duration of test. Prolong period of time for which the bearing reached thermal equilibrium was recorded for supplied pressure below 2.76 bar (40 psi). Ergo, this research is conducted with 267 N external load to the bearing rotating above 15k rpm and air is supplied above 3.45 bar.

HAFB vibration response due to impulse excitation is measured up to 30 strikes with the impact hammer each along the X (vertical) and Y (horizontal) direction for all nine cases. This enables the comparison between each data set to ensure repeatability of the measurement under specific operating condition by plotting all of the recorded vibration signals in one figure. Vibration response, following signal processing, due to X and Y impulse excitation for 18k rpm and 4.83 bar

are presented in Figure 6.1, and Figure 6.2 respectively. Observe that all the vibration signals depicted in the figure follow one similar trend which suggests repeatability of the measurements under current test apparatus setup. Referring back to Figure 4.2, impulse excitations are exerted from the top (X) and left (-Y) of the assembly with respect to front view. Therefore, vibration response in the Y (horizontal) direction shows negative values in Figure 6.1 and Figure 6.2.

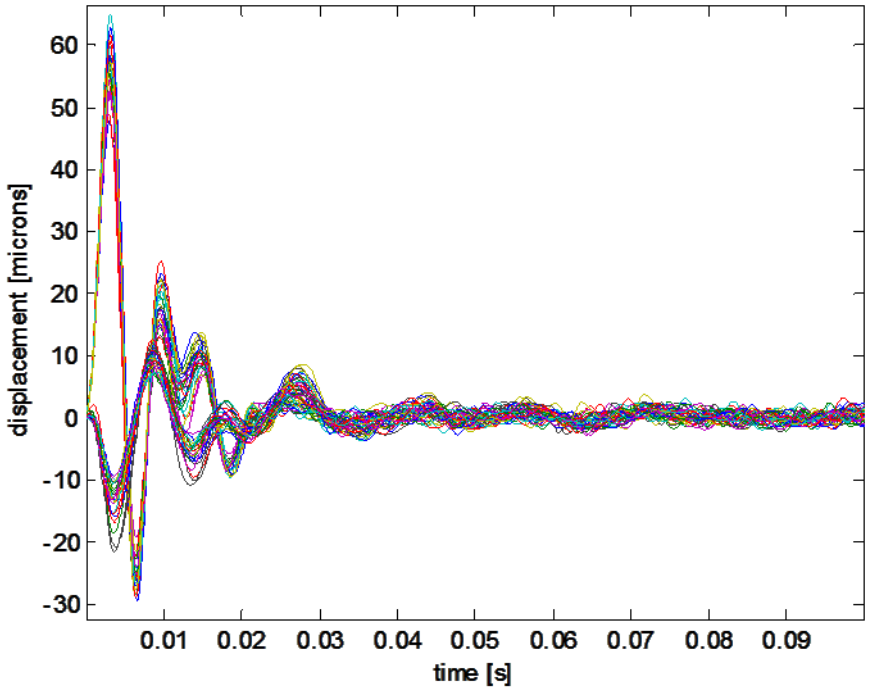

Figure 6.1 Vibration Response Due to X Impulse Excitation at 18k Rpm and 4.83 Bar Supplied Pressure.

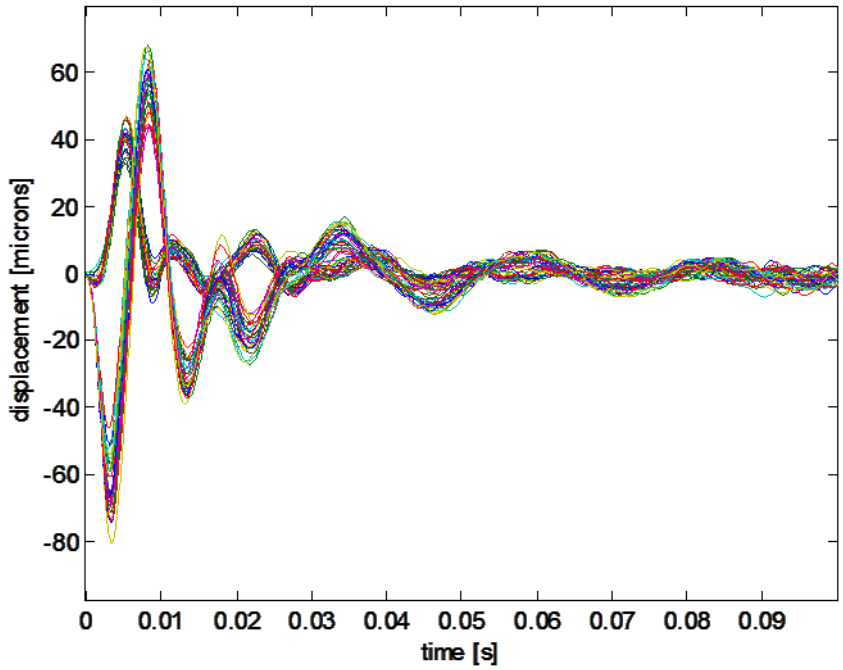

Figure 6.2 Vibration Response Due to Y Impulse Excitation at 18k Rpm and 4.83 Bar Supplied Pressure.

The least square method utilizes analysis in frequency domain. Strategically, impulse excitation and the respective vibration response are processed through Fourier Transform to decompose the signals into sets of linearly independent equations that can then be applied to multivariable regression to solve for bearing stiffness, mass, and damping coefficients. The identified coefficients for each set of vibration response therefore, consider contributions from each of the linearly independent equation at each frequency component. The resulting HAFB dynamic characteristics and mass properties listed in Table 6.1 represent average values over around 15 sets of vibration response. They are plotted against rotor speed as well as supplied air pressure in Figure 6.3 and Figure 6.4.

The identification results from experimental data are verified against results obtained under simulated environment. A rotordynamics code developed by Dr. Daejong Kim takes bearing stiffness, mass, and damping properties along with applied force and performs numerical analysis using Runge-Kutta method to simulate bearing vibration response due to given excitation. The averaged values from experimental results are entered into the program with representative excitation forces simulating magnitude similar to those applied to bearing assembly during experiments. Polynomial curve fitting in Excel was carried out to determine simulated forcing function. The bearing force coefficients identification code is then executed taking simulated vibration response as input to compare the results as well as magnitude and phase plots.

Table 6.1 HAFB Stiffness, Mass, and Damping properties

			12000	rpm	15000	rpm	18000	rpm
50 psi	Kxx	Kxy	1.54E+06	4.59E+05	1.73E+06	4.40E+05	1.93E+06	5.45E+05
	Kyx	Kyy	2.91E+05	8.96E+05	2.97E+05	9.70E+05	3.61E+05	1.20E+06
	Mxx	Mxy	3.51E+00	3.45E-01	3.33E+00	1.11E-01	3.12E+00	8.44E-02
	Myx	Myy	4.78E-01	2.93E+00	3.87E-01	2.78E+00	4.74E-01	2.90E+00
	Dxx	Dxy	1.39E+03	2.66E+02	1.68E+03	2.17E+02	1.64E+03	2.68E+02
	Dyx	Dyy	2.25E+02	5.04E+02	2.41E+02	5.89E+02	1.77E+02	7.01E+02
60 psi	Kxx	Kxy	1.65E+06	4.66E+05	1.79E+06	5.12E+05	1.94E+06	4.31E+05
	Kyx	Kyy	3.41E+05	9.84E+05	3.27E+05	9.78E+05	3.32E+05	1.02E+06
	Mxx	Mxy	3.64E+00	3.26E-01	3.46E+00	2.60E-01	3.19E+00	-2.06E-02
	Myx	Myy	5.34E-01	3.09E+00	4.57E-01	2.78E+00	4.29E-01	2.56E+00
	Dxx	Dxy	1.49E+03	2.29E+02	1.68E+03	2.21E+02	1.72E+03	2.26E+02
	Dyx	Dyy	2.44E+02	4.91E+02	1.88E+02	5.69E+02	1.75E+02	6.36E+02
70 psi	Kxx	Kxy	1.68E+06	3.92E+05	1.68E+06	4.11E+05	2.06E+06	4.02E+05
	Kyx	Kyy	2.81E+05	7.77E+05	2.84E+05	8.62E+05	3.61E+05	1.12E+06
	Mxx	Mxy	3.73E+00	2.69E-01	3.26E+00	1.76E-01	3.20E+00	-1.43E-01
	Myx	Myy	4.54E-01	2.67E+00	3.37E-01	2.53E+00	4.53E-01	2.73E+00
	Dxx	Dxy	1.43E+03	2.13E+02	1.57E+03	1.79E+02	1.63E+03	2.33E+02
	Dyx	Dyy	1.96E+02	4.22E+02	1.61E+02	5.22E+02	1.70E+02	6.36E+02

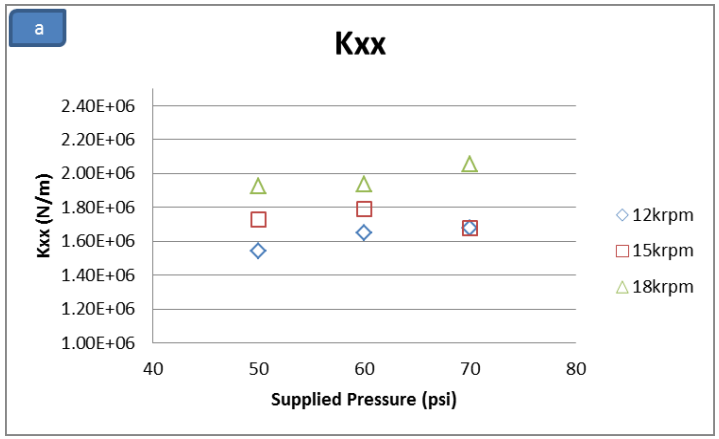

(a)

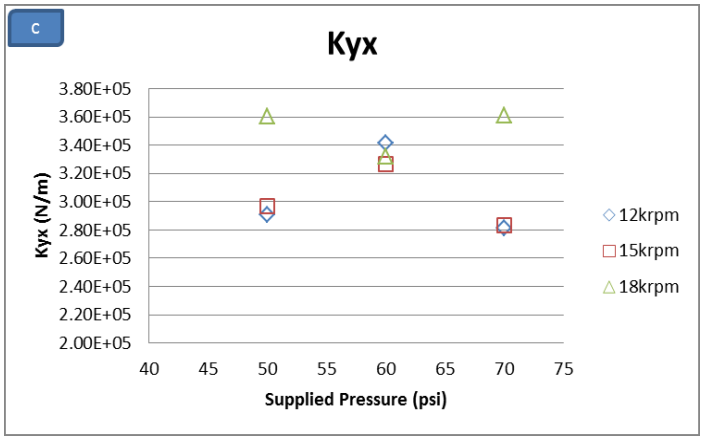

(c)

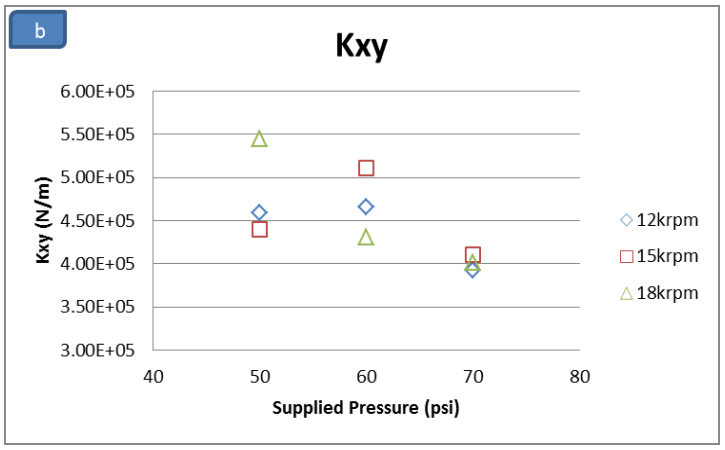

(b)

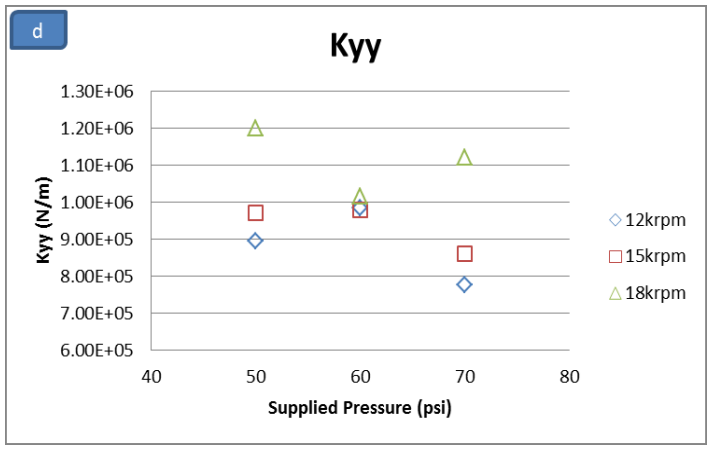

(d)

Figure 6.3 Identification Results for HAFB Direct and Crosscoupled Stiffness Coefficient showing (a) Kxx, (b) Kxy, (c) Kyx, and (d) Kyy.

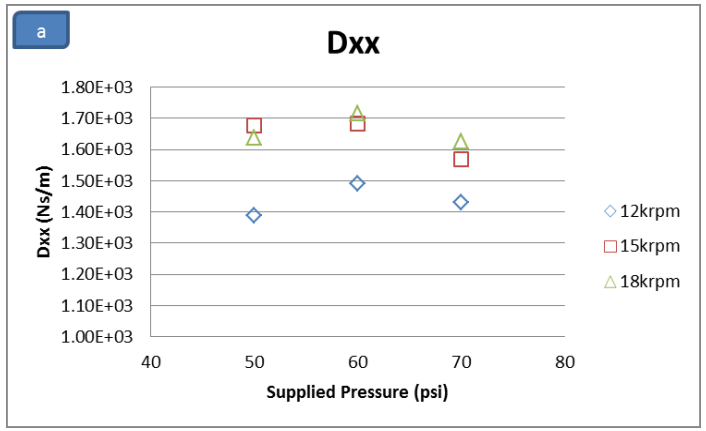

(a)

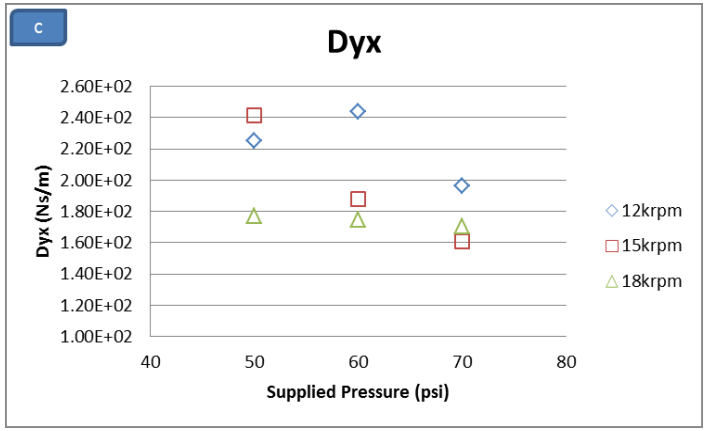

(c)

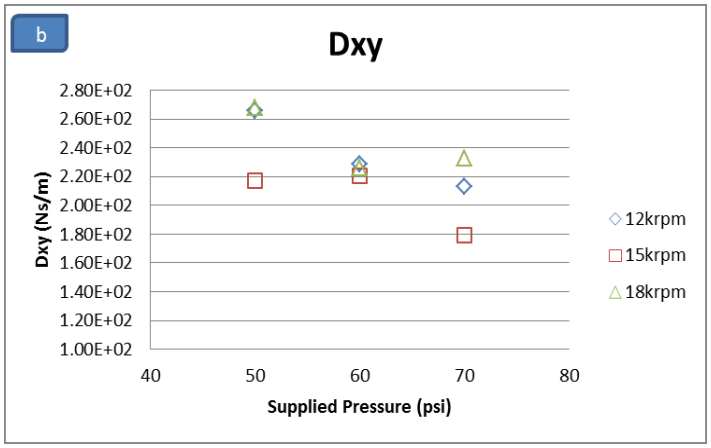

(b)

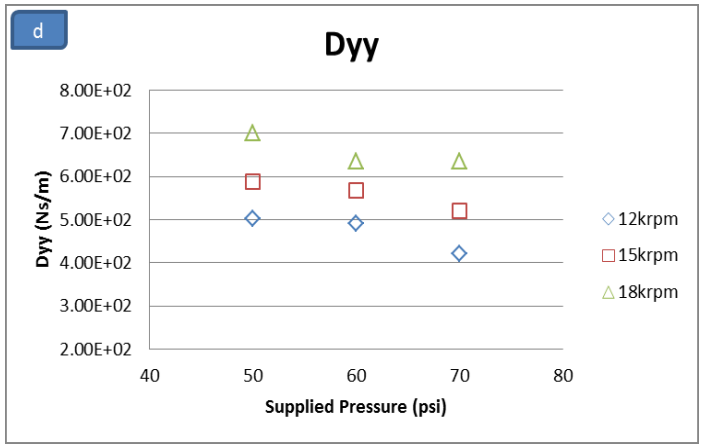

(d)

Figure 6.4 Identification Results for HAFB Direct and Crosscoupled Damping Coefficient showing (a) Dxx, (b) Dxy, (c) Dyx, and (d) Dyy.

The following figures demonstrat graphical comparison between experimental result and simulation as mentioned in the previous paragraph. Note the difference in magnitude in Figure 6.5 and Figure 6.6, although identical forces are being applied in both practices, simulated vibration seems to respond with bigger oscilations due to limitations in the physical setup that would be difficult to, and is therefore not modeled for this comparison. Nevertheless, the frequency at which the two responses oscilates and the time duration it takes for each response to reach steady state are comparable to one another. Observe in Figure 6.7, the Fourier Transform magnitude plot for experimental vibration response appears to oscilate with iregular patern due to existing noise that could not be completely eliminated with current lowpass digital filter design. Magnitude plot, is therefore, presented including higher frequency to enable comparison for system natural frequency which appear at approximately 100 Hz for both cases with simulated data presented in Figure 6.8. Similar associaton can be established regarding the comparison between Fourier Transform phase plots in Figure 6.9 and Figure 6.10. Notice that fluctuations in Figure 6.9 are 2π in magnitude that can be neglected except for the anomoly at 50 Hz for yy (bearing's horizontal vibration response due to excitation in the horizontal direction) vibration signal. The corresponding anomoly can be observed for the same signal showing high magnitude vibration at 50 Hz in Figure 6.7. This undesired vibration could be caused by difficult-to-control lingering excitation on impact.

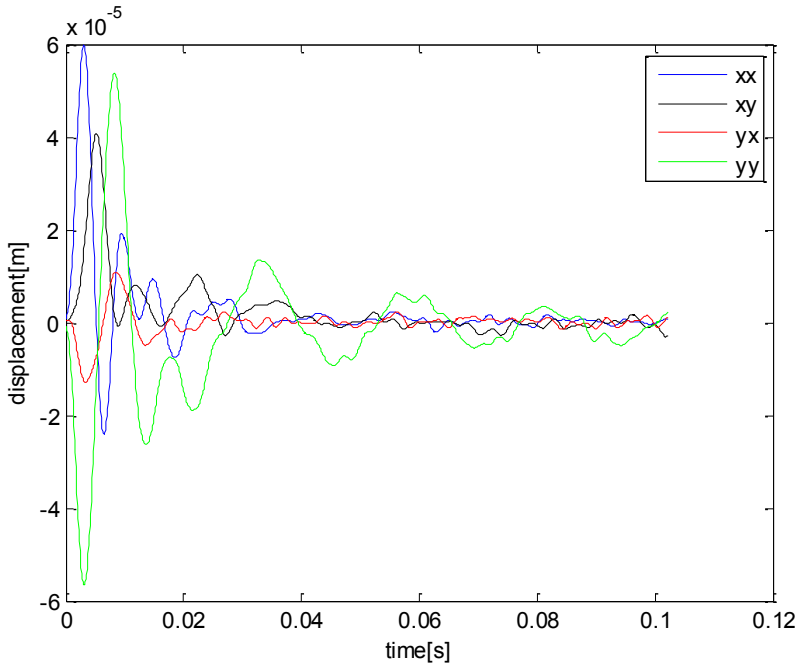

Figure 6.5 Experimental Vibration Response of HAFB at 18k Rpm and 70 Psi Supplied Pressure.

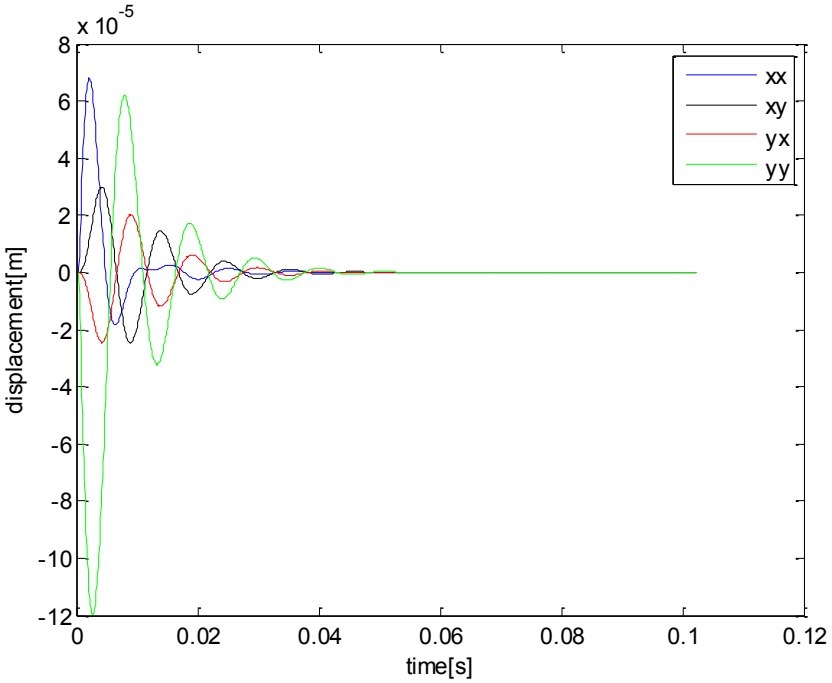

Figure 6.6 Simulated Vibration Response of HAFB Using Experiment Force Coefficients.

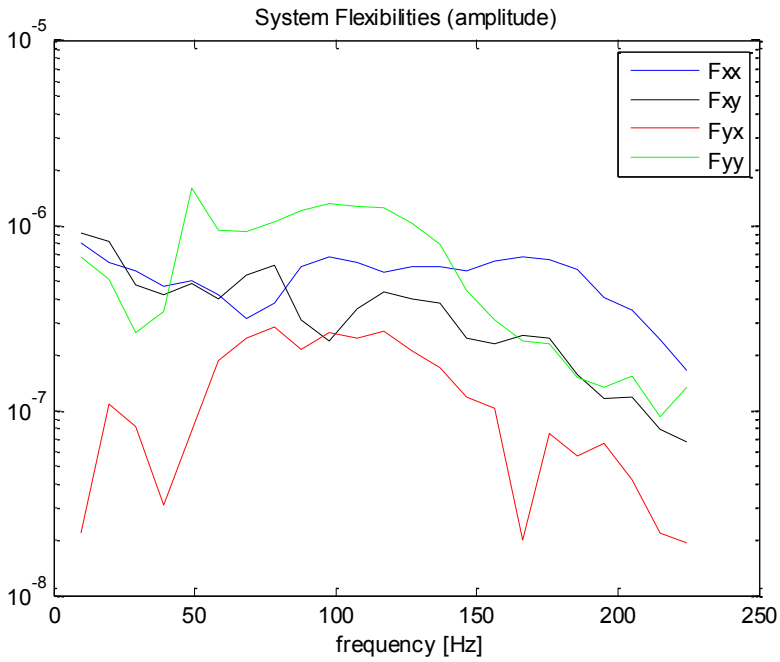

Figure 6.7 Fourier Transform Magnitude Plot of the Experimental Vibration Response.

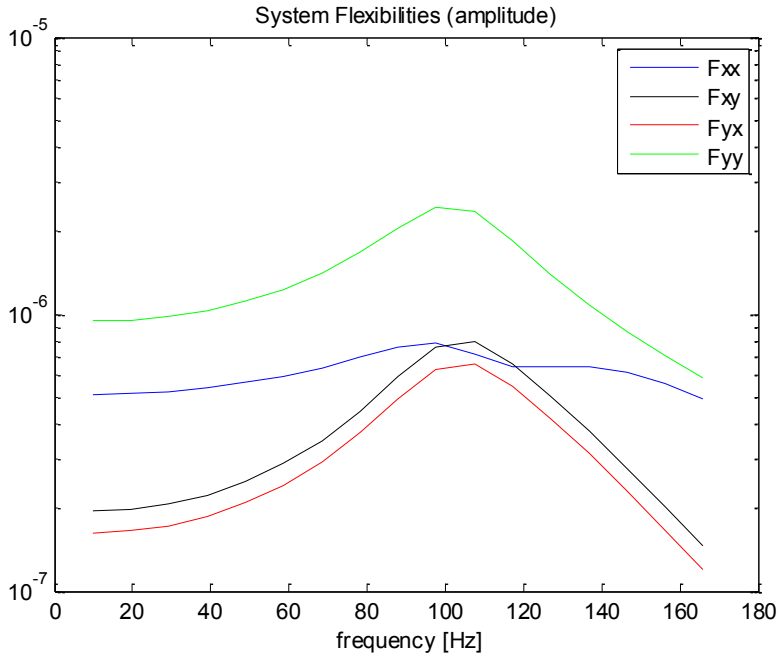

Figure 6.8 Fourier Transform Magnitude Plot of the Simulated Vibration Response.

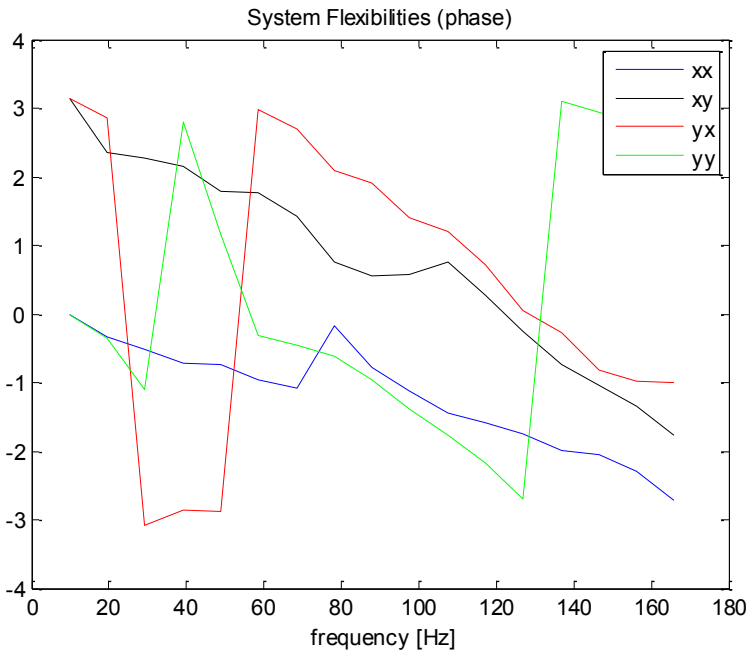

Figure 6.9 Fourier Transform Phase Plot of the Experimental Vibration Response.

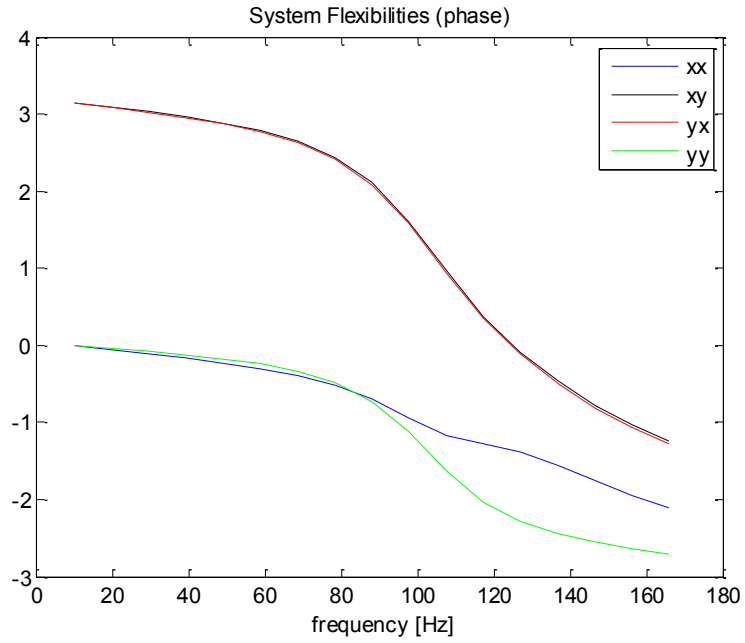

Figure 6.10 Fourier Transform Phase Plot of the Simulated Vibration Response.

From Figure 6.3, results suggest increase in direct stiffness with increasing operating speed due to growing hydrodynamic pressure buildup within the air film. This is true for both conventional hydrodynamic foil bearing and HAFB studied in this research. However, the experimental results appear to disagree with direct stiffness coefficients evaluated from analytical study. The vertical component of the direct stiffness coefficient (Kxx) ranges from 1.5 MN/m to 2 MN/m for this experiment while the same stiffness component exhibits ranges roughly one order of magnitude higher.

To explain these enormous discrepancies between experimental and analytical estimations, physical operating phenomena transpiring in current experimental setup and assumptions in analytical studies within the bearing both need to be considered. Refer back to Figure 1.1, typical foil bearings are configured with their elastic foundations in series consisting of bump toil, top foil, and existing thin fluid film within radial clearance. Due to the constricting clearance along with conceivably high speed operation, fluid film is generated with dramatically higher stiffness and therefore, the mechanical structure, namely bump foil, becomes the dictating factor when estimating stiffness characteristics of foil bearings. In practice, it is a challenging task to manufacture bump foils and top foils that perfectly conform to bearing sleeve's and rotor's contour. When partially loaded and/or existing fluid film pressure is considerably low, stiffness of the bump foil is significantly diminished like what is suspected happening in current experiment. On the other hand in analytical study, the nonconformity between foils and the circular contour of the bearing is not taken into consideration and therefore, analytical estimation predicts stiffness close to the full potential of the bump foil. Stiffness of the HAFB assembly is measured at zero running speed without hydrostatic air supply to demonstrate variation in stiffness coefficient, specifically Kxx, under various external loads. Static deformation is measured with proximity probes with 10 lb. increments. The results along with 3rd order polynomial approximation curve are shown in Figure 6.11 and Table 6.2 tabulates static stiffness coefficients evaluated from the first order derivative of the approximated curve. Observe the dramatic increase in bearing

stiffness from 50 lb. to 60 lb. applied load and recall the test rig is loaded below 50 lb. for the identification of bearing dynamic characteristics.

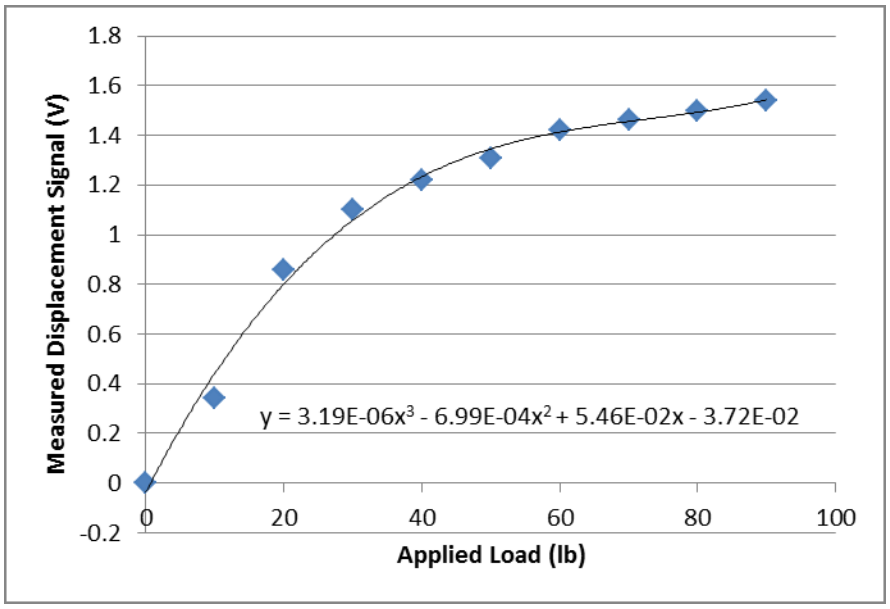

Figure 6.11 HAFB Static Deformation Curve.

Table 6.2 HAFB Static Stiffness

Tot_load (lb)	Kxx (N/m)
10	8.86E+05
20	1.16E+06
30	1.59E+06
40	2.28E+06
50	3.46E+06
60	5.61E+06
70	9.36E+06
80	1.33E+07
90	1.21E+07
100	7.69E+06

In addition, it is of interest to this study to gauge how the experimental results compare to previous analytical efforts in terms of the sensitivity in bearing force coefficients to changes in rotor speed and supplied pressure in particular. Referring back to literature review presented in Section 2.5, previous analytical investigation on HAFB dynamic characteristics showed decreased cross-coupled stiffness with increasing rotor speed. Also, the results discussed in Section 2.6 suggests higher onset of rotor instability for HAFB with the introduction of hydrostatic pressure.

From b and c, however, it is difficult to establish the equivalent claims for cross-coupled stiffness with increasing supplied pressure. Recall the identification results presented in Table 6.1 represent the average over approximately 15 different excitation responses. Error bar interpretation of the deviation of each value from their averaged value reflects no significance when standard deviation is large. The identifications for all nine different cases investigated in this study show typical standard deviation that is roughly 15% or less of the average value for direct stiffness/damping and 25% to 35% of the average value for cross-coupled stiffness/damping. Consequently, it is difficult to induce reasonable interpretation from the identification data with only 15 data sets. Nevertheless, while variation in supplied pressure does not appear to have significant impact on damping characteristics of the bearing, the identification results seem to indicate general decrease in cross-coupled damping with increase rotor speed, and the opposite is shown for direct damping that increases with rotor speed.

CHAPTER 7

CONCLUSION AND FUTURE WORK

The scope of the current study consists of numerous tasks; manufacture of the bearing, bearing assembly, test apparatus setup, development of LabVIEW data acquisition program, signal processing, and ultimately application of least square method for the identification of force coefficients for the hybrid air foil bearing (HAFB). Literature reviews are summarized to provide fundamental understanding of foil bearing in operation and the benefits of HAFB that combines hydrostatic lift with hydrodynamic effect. They are also presented in this paper for validation of HAFB design as well as comparison between experimental and analytical results.

Experimental procedures are modified based on data interpretation. Baseline subtraction must be engaged prior to signal filtering in order to accurately pinpoint phase lag between impact excitation and synchronous baseline signal. Hydrostatic pressure is applied on both ends of the bearing to constrain sliding motion in the axial direction when the rotor is lifted at the tested speeds. To streamline identification effort, signal processing program is created taking raw vibration response as input, transforming the data through baseline subtraction and signal filtering, then proceed to saving individual vibration response that is plotted to verify repetition of measurements.

Supplementary rotordynamics program developed by Dr. Daejong Kim is used for the confirmation of experimental results. It is pointed out in the previous chapter that simulated vibration magnitude appears to be larger because radial constraints were not modeled in the simulation, yet the resulting vibration response taking experimentally identified bearing properties and equivalent simulated impact excitation produces comparable vibration frequency as well as elapsed time before reaching steady state.

Vibration response is measured under 12k, 15k, and 18k rpm supplying 50, 60, and 70 psi air pressure. Experimentally identified bearing stiffness and damping coefficients are applied to the rotordynamics simulation and verifications are performed for all nine operating conditions. Further understanding of the impact of how the bearing structure physically sit within the assembly on bearing performance is examined to clarify the massive discrepancy between analytically identified and experimentally identified bearing stiffness. Static deformation test is performed to demonstrate significant variation in direct stiffness as indicated in the preceding chapter. Furthermore, experimental results are compared with previous parametric study in terms of how variations in rotor speeds and supplied hydrostatic pressure change bearing elastic properties. Data displayed suggests ambiguous tendencies, and it is problematic to reflect on the significance of the comparison to analytical investigations when standard deviations are perceivably large. There are numerous factors that could have effects on the precision of measurements conducted in this investigation. Hybrid air foil bearing elastic structures are fabricated by hand and any manufacturing flaw can have substantial impact on bearing performance when foils do not sit properly along the bearing holder and/or when hydrostatic air flows are not uniform. Consequently, cross coupled components of bearing dynamic properties are usually difficult to identify.

To remedy concerns for accuracy of the results due to large standard deviation, impulse excitation response should be measured sufficient number of times before taking average. Furthermore, the data presented in this paper for stiffness and damping coefficients represents a frequency averaged evaluation and any irregular vibration response exists within the cutoff frequency can deteriorate experiment results. In the future, it's desirable to replace current excitation source with a pair of electromagnetic shakers that can stimulate the bearing to vibrate at controlled frequency. The application of electromagnetic shakers will allow identification of the bearing stiffness and damping coefficients at distinct frequencies and hence dramatically improve accuracy of the identification results.

APPENDIX A

MULTIVARIABLE REGRESSION

Assuming there is a set of measured data:

$$\text{independent variable: } \begin{cases} x_i \\ y_i \end{cases},$$

$$\text{dependent variable: } z_i$$

$$i = 1, 2, 3, ..., n$$

And consider the relationship of the following form

$$z_i = ax_i^2 + bx_i + cx_i y_i^2 + dx_i y_i$$

$$\begin{bmatrix} z_1 \\ z_2 \\ \vdots \\ z_n \end{bmatrix} \quad \begin{bmatrix} x_1^2 & x_1 & x_1 y_1^2 & x_1 y_1 \\ x_2^2 & x_2 & x_2 y_2^2 & x_2 y_2 \\ \vdots & \vdots & \vdots & \vdots \\ x_n^2 & x_n & x_n y_n^2 & x_n y_n \end{bmatrix} \begin{bmatrix} a \\ b \\ \\ d \end{bmatrix}$$

$$\Rightarrow [\quad] \quad [\quad][\quad]$$

$[\vec{z}]: n \times 1$, $[X]: n \times 4$, *and* $[\vec{a}]: 4 \times 1$

Note $[\vec{a}]=[X]^{-1}[\vec{y}]$ is not allowed since $[X]$ is not a square matrix

Define:

$$[X]^T [X] = [K]$$

$$[K]: 4 \times 4$$

$$\Rightarrow [X]^T [\quad] = [\quad][\quad]$$

Through algebraic manipulation:

$$[\quad] = [\quad]^{-1} [\quad] [\quad] \quad [\quad] = (\quad)^{-1} [\quad] [\quad]$$

The resulting $[\quad]$ matrix gives the regression coefficients that minimize the square deviation.

APPENDIX B

DATA ACQUISITION WITH LABVIEW

LabVIEW VI is constructed for impulse response data collection. Both front panel view and block diagram are shown here. Instead of recording continuous time signal, a trigger mechanism is utilized to initiate data acquisition at the onset of each impulse excitation for a user defined number of samples to record. A live display for load cell is added to the front panel view to monitor friction generated within the hybrid air foil bearing during non-zero speed operations. Filtered and raw proximity probe signals are both triggered by the impulse excitation to show live display in the front panel view. Control buttons enable users to switch on/off data collection.

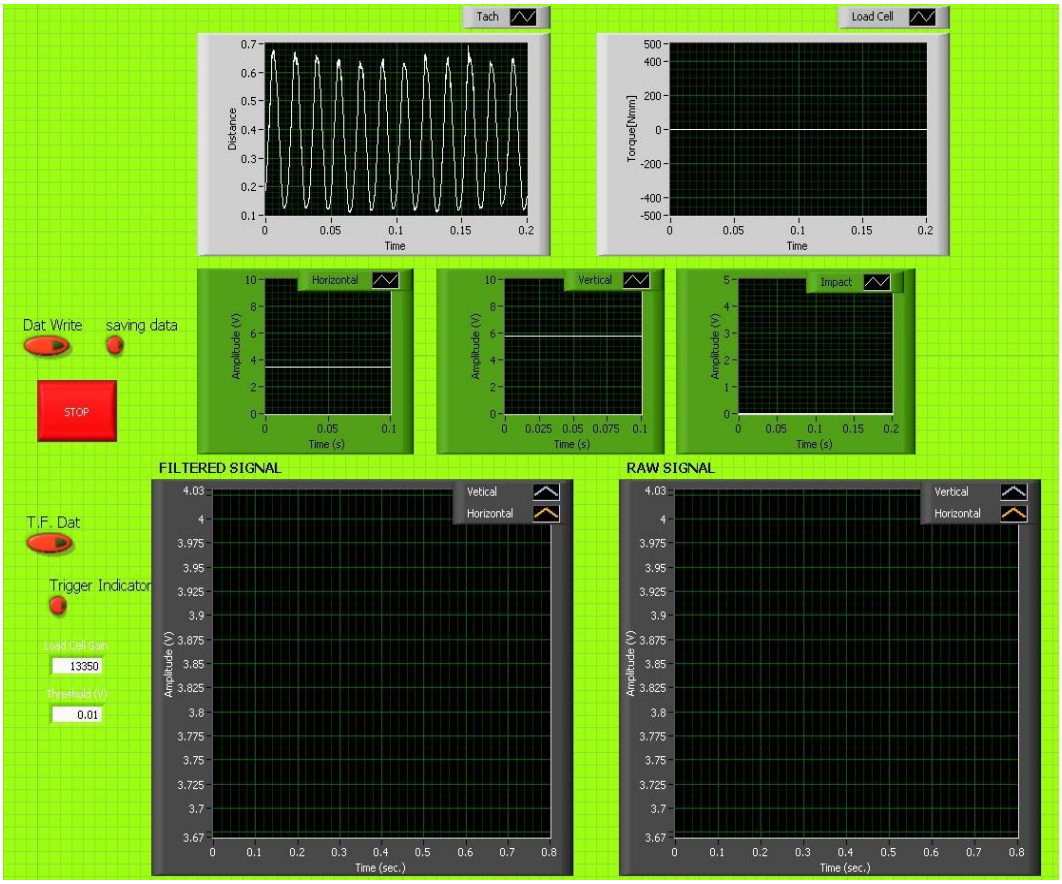

Figure B1. LabVIEW VI Front Panel View.

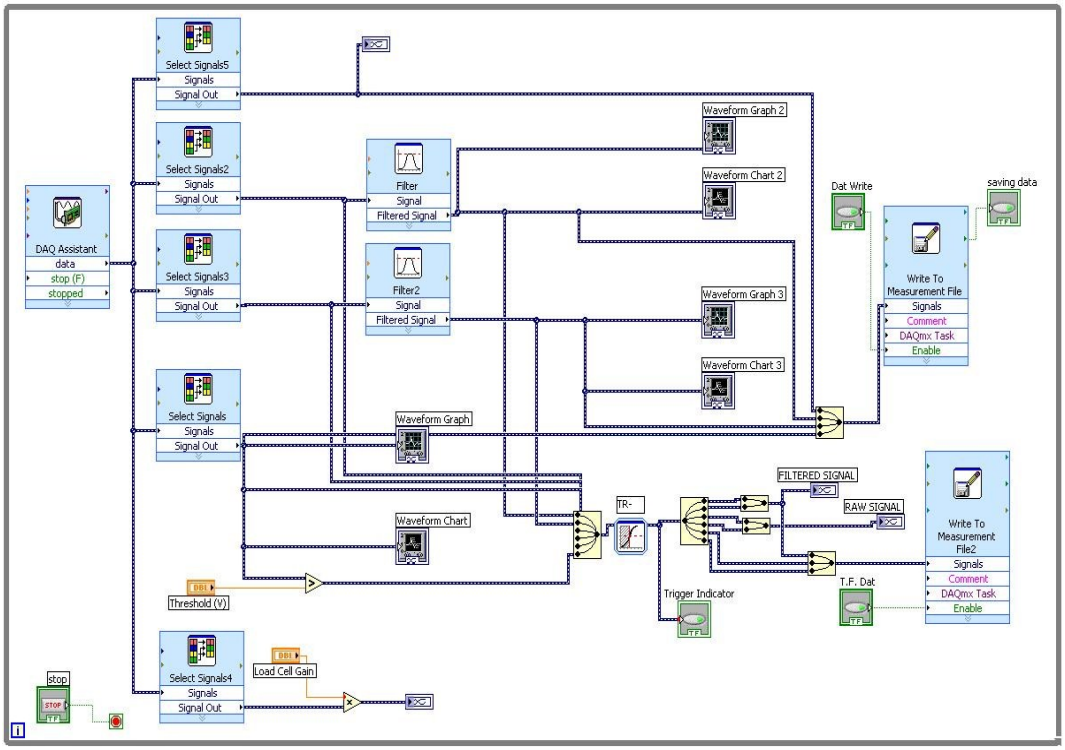

Figure B2. LabVIEW VI Block Diagram.

REFERENCES

[1] Agrawal, G. L., 1997, "Foil Air/Gas Bearing Technology -- an Overview," International Gas Turbine & Aeroengine Congress & Exhibition, Orlando, FL, June 2-June 5,1997, ASME Paper No. 97-GT-347.

[2] Radil, K., and Zeszotek, M., 2004, "An Experimental Investigation into the Temperature Profile of a Compliant Foil Air Bearing," STLE Tribology Transactions**, 47**(4), pp. 470-479.

[3] Radil, K., DellaCorte, C., and Zeszotek, M., 2007, "Thermal Management Techniques for Oil-Free Turbomachinery Systems," STLE Tribology Transactions**, 63**(10), pp. 319-327.

[4] Kim, D., and Lee, D., 2010, "Design of Three-Pad Hybrid Air Foil Bearing and Experimental Investigation on Static Performance at Zero Running Speed," Journal of Engineering for Gas Turbine and Power**, 132**(12), pp. 122504-1~10 (10 pages), DOI:10.1115/1.4001066.

[5] Heshmat, H., 2006, "Evaluation of Coatings for a Large Hybrid Foil/MagneticBearing," ASME Paper no. IJTC2006-12328.

[6] Kim, D., and Park, S., 2006, "Hybrid Air Foil Bearing with External Pressurization," ASME Journal of Tribology, , pp. 63-69.

[7] Radil, K., Howard, S., and Dykas, B., 2002, "The Role of Radial Clearance on the Performance of Foil Air Bearings," STLE Tribology Transaction**, 45**(4), pp. 485-490.

[8] Kim, D., 2007, "Parametric Studies on Static and Dynamic Performance of Air Foil Bearings with Different Top Foil Geometries and Bump Stiffness Distributions," ASME Journal of Tribology**, 129**(2), pp. 354-364.

[9] Kumar, M., and Kim, D., 2008, "Parametric Studies on Dynamic Performance of Hybrid Air Foil Bearings," Journal of Engineering for Gas Turbines and Power**, 130**(6), pp. 062501-1-062501-7.

[10] Kim, D., and Zimbru, G., 2012, "Start-Stop Characteristics and Thermal Behavior of A Large Hybrid Airfoil Bearing for Aero-Propulsion Applications," ASME Journal of Engineering for Gas Turbine and Power**, 134**(3), pp. 032502 (9 pages).

[11] Diaz, S. E., and San Andrés, L., 1999, "A METHOD FOR IDENTIFICATION OF BEARING FORCE COEFFICIENTS AND ITS APPLICATION TO A SQUEEZE FILM DAMPER WITH A BUBBLY LUBRICANT," STLE Tribology Transactions**, 42**, pp. 739.

[12] Qiu, Z. L., and Tieu, A. K., 1997, "Identification of Sixteen Force Coefficients of Two Journal Bearings from Impulse Responses," WEAR, pp. 206-212.

BIOGRAPHICAL INFORMATION

Yu Ping Wang received his Bachelor of Science degree in Mechanical and Aeronautical Science Engineering as well as a minor in Managerial Economics from University of California, Davis. He joined the Microturbomachinery and Energy System Lab guided by Dr. Daejong Kim in 2011 while pursuing his Master of Science degree in Aerospace Engineering at University of Texas, Arlington. He was the accompanying fellow joining with Dr. Daejong Kim in the 2011 Summer Faculty Fellowship Program at the Wright Patterson Air Force base where he commenced his research work involving experimental identification of bearing dynamic characteristics. Friendship, hard work, experience, and creativity have been the four most treasured values throughout his college career and he is looking forward to even more exciting opportunities in the future where he can further improve his knowledge and skill in the aerospace industry.